

Phosphorus dynamics in and below the redoxcline in the Black Sea and implications for phosphorus burial

N. Dijkstra^{a,*}, P. Kraal^a, M.J.M. Séguret^a, M.R. Flores^a, S. Gonzalez^b,
M.J.A. Rijkenberg^c, C.P. Slomp^a

^a Department of Earth Sciences – Geochemistry, Faculty of Geosciences, Utrecht University, PO Box 80021, 3508 TA Utrecht, The Netherlands

^b NIOZ Royal Netherlands Institute for Sea Research, Department of Marine Microbiology and Biogeochemistry (MMB), and Utrecht University, PO Box 59, 1790 AB Den Burg, Texel, The Netherlands

^c NIOZ Royal Netherlands Institute for Sea Research, Department of Ocean Systems (OCS), and Utrecht University, PO Box 59, 1790 AB Den Burg, Texel, The Netherlands

Received 31 March 2017; accepted in revised form 12 November 2017; available online 20 November 2017

Abstract

Marine basins with oxygen-depleted deep waters provide a natural laboratory to investigate the consequences of anoxic and sulfidic (i.e. euxinic) conditions for biogeochemical processes in seawater and sediments. In this study, we investigate the dynamics of the key nutrient phosphorus (P) and associated elements such as manganese (Mn), iron (Fe) and calcium (Ca) in the euxinic deep basin of the Black Sea. By examining water column particles with scanning electron microscope – energy dispersive spectroscopy and synchrotron-based X-ray absorption spectroscopy, we show that Mn(III/IV)-P is the key form of particulate P in the redoxcline. Other forms of particulate P include organic P, Fe(III)-P, and inorganic polyphosphates. Most inorganic P particles that are formed in the redoxcline subsequently dissolve in the underlying sulfidic waters, with the exception of some particulate Fe(III)-P that accounts for <1% of all P settling onto the seafloor. Organic P is the dominant source of P to the sediment. Most of this organic P is degraded in the upper 2 cm of the sediment. Results of sequential extractions and a ³³P radiotracer experiment point towards the formation of labile Ca-P and P adsorbed onto calcium-carbonate and clays and a role of these phases as a major sink of P in the sediment. The total P burial efficiency in the sediments is ~27%, which is relatively high when compared to estimates for sediments in other euxinic basins such as the Baltic Sea (<12%). We suggest that the abundant presence of calcium carbonate may contribute to the more efficient sequestration of P in Black Sea sediments.

© 2017 Elsevier Ltd. All rights reserved.

Keywords: Particulate P; Organic P; Calcium-associated P; Redox chemistry; Black Sea

1. INTRODUCTION

Oxygen concentrations in many coastal waters have been decreasing since the 1960s, resulting in an expansion of so-called dead zones where oxygen concentrations in bottom waters are below 2 mg/L (Diaz and Rosenberg,

2008; Rabalais et al., 2014). One of the primary causes for expansion of dead zones is the enhanced riverine input of nutrients from fertilizers, which stimulates primary productivity in coastal surface waters and increases the oxygen demand in deep waters linked to remineralization of the excess organic matter (Diaz and Rosenberg, 2008; Rabalais et al., 2014). An example of such a coastal human-induced dead zone is the Baltic Sea (Conley et al., 2009; Carstensen et al., 2014), where more than 60,000

* Corresponding author.

E-mail address: n.dijkstra@uu.nl (N. Dijkstra).

km² of bottom waters are seasonally or even permanently hypoxic, anoxic or euxinic (i.e. <2 mg O₂/L, no oxygen or free dissolved sulfide (referred to as HS[−]) in bottom waters, respectively).

Bottom water euxinia in restricted basins such as the Cariaco Basin and the Black Sea occurs naturally due to stable water column stratification that limits vertical mixing in the water column and thereby decreases the supply of oxygen to the deep waters (Degens and Ross, 1974; Wilkin et al., 1997; Arthur and Dean, 1998; Scranton et al., 2001). These euxinic basins provide a natural laboratory to investigate the consequences of low oxygen conditions on biogeochemical cycling in the water column and sediments. While many studies have investigated the carbon (C), manganese (Mn), iron (Fe) and sulfur (S) dynamics in these basins (Fry et al., 1991; Calvert et al., 1996; Wijsman et al., 2001; Trouwborst et al., 2006), the dynamics of the key nutrient phosphorus (P) in the water column and surface sediments are less well understood.

The potential carriers of P towards the seafloor in euxinic basins consist of both organic and inorganic particles (Benitez-Nelson et al., 2007; McParland et al., 2015). Euxinic basins are particularly enriched in inorganic P in or close to the redoxcline (i.e. the water layer that separates oxic surface waters from sulfidic deep waters). This is, in part, caused by a close coupling between the dynamics of particulate Mn, Fe and P (Dellwig et al., 2010). The redoxcline is typically enriched in Mn(IV) oxides such as birnessite (δ-MnO₂), which undergo reductive dissolution when sinking into deeper sulfidic waters (Tebo, 1991; Tebo et al., 2004). A portion of the released Mn²⁺ diffuses upwards into the redoxcline and is again oxidized to form Mn oxides, thereby driving a Mn pump in the water column. The cycling of Fe in the water column is also driven by redox reactions but, in contrast to Mn, a distinct maximum in particulate Fe(III) (oxyhydr)oxide (Fe oxide) is not always present in the redoxcline (Lewis and Landing, 1991; Pakhomova et al., 2009). Phosphate (henceforth termed PO₄) can bind to Mn and Fe particles, resulting in the presence of Mn-Fe-P phases within the redoxcline (Dellwig et al., 2010). In addition to these mixed particles, colloidal complexes containing Mn(III) and pyrophosphate (simplified as Mn(III)-P) can contribute to the particulate P pool in the redoxcline of the Black Sea (Yakushev et al., 2007, 2009). The formation and dissolution of Mn-Fe-P particles is assumed to be responsible for the classical structure in PO₄ depth profiles in euxinic basins with a minimum in PO₄ where oxygen becomes depleted and a PO₄ maximum at the depth where HS[−] starts to accumulate (Shaffer, 1986; Dellwig et al., 2010; Yakushev et al., 2009). Particulate Fe(III) and Mn(III/IV) are highly susceptible to HS[−]-induced dissolution. Half-life times for reactive Fe oxides (except magnetite) in sulfidic waters are less than 30 days (Canfield et al., 1992) and Mn(IV) oxides quickly dissolve in the presence of HS[−] (<10 min.; Burdige and Nealson, 1986). In addition, Mn(III)-P complexes dissolve within seconds in sulfidic waters (Kostka et al., 1995). In euxinic basins where particles experience long HS[−] exposure times, most particulate Mn-Fe-P is thus assumed to undergo reductive dissolution before reaching the seafloor

(Dellwig et al., 2010). Recent studies in deep euxinic basins in the Baltic Sea and Black Sea (water depth > 170 m below sea surface (mbss)) suggest, however, that some Mn oxides and Fe oxides can survive transport through a euxinic water column and may act as a carrier of P towards the seafloor (Jilbert and Slomp, 2013; Dijkstra et al., 2014, 2016).

In addition to Mn-Fe-P phases, redoxclines can be enriched in inorganic polyphosphates (i.e. linear polymers of three to several hundred PO₄ groups; Kornberg, 1995), as has recently been shown for Effingham Inlet, a restricted anoxic fjord off the west coast of Vancouver Island (Diaz et al., 2012). These inorganic polyphosphates do, however, dissolve when entering deeper anoxic waters, presumably due to anoxic remineralization (Diaz et al., 2012). This is in line with other studies that show a release of PO₄ from polyphosphates under reducing conditions (Sannigrahi and Ingall, 2005; Schulz and Schulz, 2005; Brock and Schulz-Vogt, 2011).

Other forms of particulate P phases are less sensitive to dissolution in sulfidic waters than Mn-Fe-P and inorganic polyphosphates. These are, for instance, biogenic hydroxypapatites (Schenau and De Lange, 2000; Slomp et al., 2002) and detrital apatites (Ruttenberg, 2003). Sediments below sulfidic waters can also contain carbonate fluorapatite (e.g. Mort et al., 2010). These apatites may form in the water column in micro-environments in large sinking particles (Faul et al., 2005) and can precipitate *in-situ* in the sediment as suggested for the deep Black Sea (Dijkstra et al., 2014; Kraal et al., 2017). In sulfidic calcium-carbonate (CaCO₃)-rich sediments, P associated with CaCO₃ can be an additional important P burial phase besides organic P (Kraal et al., 2017). The formation of CaCO₃-P may already occur in the overlying water column via adsorption of PO₄ onto biogenic CaCO₃, as has been proposed for the oxic Ems estuary (De Jonge and Villerius, 1989). In addition to carbonates, PO₄ can also be adsorbed to clays (Krom and Berner, 1980) but their role as a carrier of P towards in the seafloor in sulfidic basins has not yet been investigated.

While the dynamics of P in and around the redoxcline in euxinic basins have been intensively studied (e.g. Dellwig et al., 2010; Yakushev et al., 2009), the carriers of P towards the seafloor in such basins are still undetermined. The susceptibility to reaction with HS[−] differs between P phases and with it the extent to which the various P phases survive transport through sulfidic waters. Thus, the nature of the P particles in the water column can determine the rate of P deposition and, ultimately, the burial of P in the sediment.

In this study, we investigate the dynamics of Fe, Mn, Ca and P in the water column and in the surface sediment at a site in the euxinic deep basin of the Black Sea using bulk geochemical analyses, ³³P radiotracer experiments with surface sediments and detailed analysis of particles with scanning electron microscope – energy dispersive spectroscopy (SEM-EDS) and synchrotron-based X-ray absorption spectroscopy (XAS). We demonstrate that organic P is likely the major carrier of P to the seafloor. Most of the incoming organic P is degraded in the surface sediment. We further find evidence for an important role for CaCO₃ in P sequestration in the deep

basin sediments, possibly through the formation of adsorbed P, labile Ca-P and authigenic Ca-P.

2. METHODS

2.1. Study site and sample collection

The Black Sea experiences permanent sulfidic bottom waters below ~150 m water depth (>7000 years; [Ross and Degens, 1974](#); [Calvert et al., 1996](#); [Wilkin et al., 1997](#); [Arthur and Dean, 1998](#)). The deep central basin in the Black Sea is density-stratified with a stable redoxcline that separates sulfidic and relatively saline deep waters from oxic and less saline surface waters. Most freshwater discharge takes place on the north-western shelf of the Black Sea through the rivers Danube, Dniester and Dnieper ([Tolmazin, 1985](#)). Our station 2 in the deep basin (N 42° 53.8', E 30°40.7'; [Fig. 1](#)) is overlain by a 2107 m water column.

Station 2 was visited with RV Pelagia in June 2013. Water samples were collected using a conductivity-temperature-depth (CTD) rosette with 24 Niskin bottles and sensors to continuously measure conductivity, temperature, fluorescence, beam transmission and dissolved oxygen. After collection of the water samples, the remaining water from each depth (10–20 L) was filtered through 0.2 µm Isopore polycarbonate membrane filters (147 mm). In order to avoid oxidation of the collected particles, the filters were placed into air-tight Geotech polycarbonate filter holders in a glovebag and all tubing was purged with nitrogen gas and subsequently rinsed with deoxygenated ultrapure water prior to filtration. Immediately after finishing filtration of a series of CTD bottles, the filter holders with filters were transferred to a nitrogen-purged glovebag in a cold room (10 °C). The filters were removed from the holder and stored at –20 °C in air-tight jars until microanalysis. In addition, McLane WTS-LV in-situ pumps were

deployed to collect particles on pre-combusted glass fibre filters (GFF; 0.7 µm pore size, 142 mm diameter). Flowmeters were used to register the volume of filtered water for each in-situ pump. The filters were wrapped in aluminium (Al) foil after retrieval under normal atmosphere and were directly stored at –80 °C until analysis. Sediment cores were collected at station 2 using a multi coring device equipped with 60 cm-long polycarbonate tubes. Sediments were sectioned at a depth resolution of 0.5–4 cm in a nitrogen-purged glovebag, transferred to glass vials and transported at 4 °C to Utrecht University.

Station 2 was revisited in September 2015 with RV Pelagia to collect water samples for dissolved Fe measurements using ultra-trace metal clean PVDF samplers with a Kevlar hydrowire ([De Baar et al., 2008](#); [Rijkenberg et al., 2014](#)). No distinct differences in water column characteristics (e.g. oxygen, HS[–] and PO₄) were observed between the 2013 and 2015 sampling campaigns ([Appendix A](#)). In addition, McLane in-situ pumps (3 × WTS-LV; 1 × WTS-LV Dual Filter) with 0.8 µm Supor filters (142 mm) were deployed at 11 water depths to collect particles for sequential P extractions. Eight water depths (60, 80, 95, 105, 110, 120, 140, 500 mbss) were sampled with WTS-LV pumps and three water depths (170, 250 and 2000 mbss) were sampled with the WTS-LV Dual pump. The filters on the WTS-LV pumps were collected immediately after the pumps were retrieved and stored in nitrogen-purged Al-bags (gas-tight Al-laminate lined with plastic on the inside, Grueber Folien GmbH). The filters on the WTS LV Dual Filter pump were covered with Black Sea water during retrieval and thus shielded from the atmosphere. These filters were removed from the filter holders in a nitrogen-purged glovebag and directly stored in nitrogen-purged Al-bags. All filters were kept at –20 °C until analysis at Utrecht University. Sediment for the ³³P radiotracer incubations was collected in 2015 at station 2 and, for comparison, at station 9 on the oxic shelf (27 mbss; 44°34.9'N-29°11.38'E).

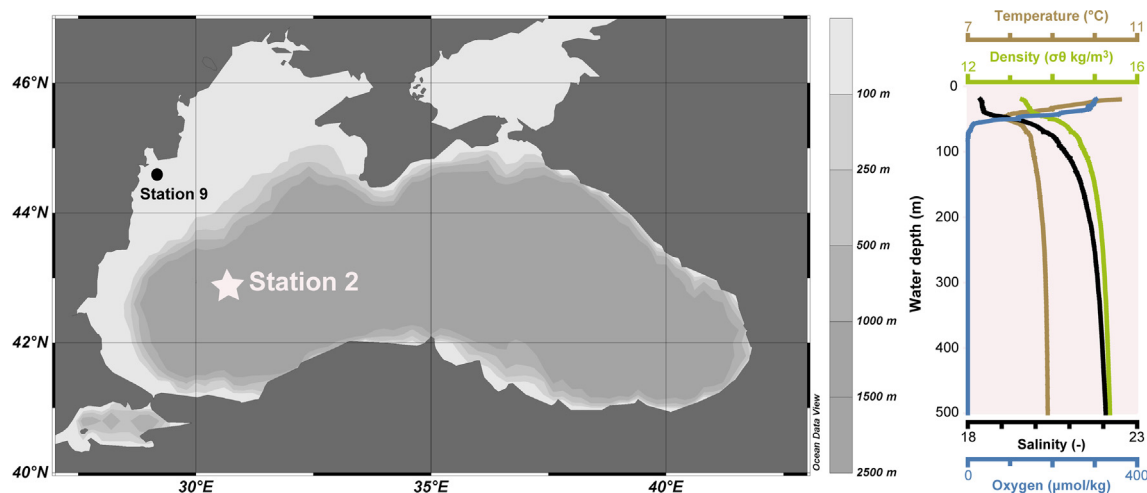


Fig. 1. Locations of stations 2 and 9 and water column characteristics at station 2. The temperature, density, oxygen concentration and salinity for the upper 500 m of the water column for June 2013 are shown. Similar trends with depth were observed in September 2015 (see [Appendix A](#) for comparison). The water column properties show little change with water depth below 500 m (not shown).

2.2. Water column analyses

After retrieval, the water in the CTD rosette bottles was immediately sampled, filtered (0.45 μm Teflon filter) and analysed on-board for dissolved PO_4 and HS^- with Quattro gas-segmented continuous flow analysers (Murphy and Riley, 1962; Grasshoff et al., 1983). The relative standard deviation based on duplicate samples was generally below 4% for PO_4 and below 10% for HS^- . A small aliquot of the filtered water from each CTD bottle was acidified and stored (4 $^\circ\text{C}$) until further analysis. At Utrecht University, the acidified samples were diluted three times with 1M HCl (Ultrapure). Total dissolved Mn (dMn) was measured by inductively coupled plasma – optical emission spectrometry (ICP-OES; SPECTRO ARCOS). The detection limit for undiluted samples was 0.33 μM Mn. Methodology and water column profiles for ammonium (NH_4^+), nitrate (NO_3^-) and nitrite (NO_2^-) are shown in Appendix A.

For the determination of dissolved Fe, 0.5 L of seawater was filtered through a 0.2 μm Sartobran 300 cartridge with a cellulose acetate membrane (Sartorius) under nitrogen pressure and collected in acid-washed 60 mL LDPE bottles (NalgeneTM). These bottles were acidified to pH 1.8 using distilled HCl and stored at 4 $^\circ\text{C}$ prior to analysis at Utrecht University. Total dissolved Fe (dFe) was measured by flow-injection with chemiluminescence with preconcentration detection (Klunder et al., 2011; Rijkenberg et al., 2014). All triplicate samples from a station were analysed from surface waters to depth during the same run. The detection limit was 0.025 ± 0.012 nM. The accuracy of the system was measured daily using GEOTRACES reference material D1, 0.65 ± 0.04 nM, consistent with the community consensus value of 0.64 ± 0.04 nM (Johnson et al., 2007).

2.3. Analysis of particles on GFF filters

An oven-dried (60 $^\circ\text{C}$) GFF filter piece from each depth was digested overnight in a mixture of hydrofluoric acid, nitric acid and perchloric acid solution at 90 $^\circ\text{C}$. After the acids were fumed off the next day, the residues were dissolved in 1M nitric acid. Total Mn concentrations in the solutions were measured by ICP-OES whereas total P and total Fe concentrations were measured colorimetrically by the molybdenum blue method (Strickland and Parsons, 1972) and the phenanthroline method (APHA, 2005), respectively. All concentrations were corrected for background concentrations with duplicate filter blanks. The detection limit was 1.3 nM for Mn, 4.3 nM for P and 2.1 nM for Fe ($3 \times$ blank standard deviation). We were not able to conduct the analysis in duplicate due to insufficient filter material. No data was available for particulate P from the 2000 mbss GFF filter. We therefore determined the P concentration at 2000 mbss by total destruction and ICP-OES of a piece of the Isopore filter from the Niskin bottles (blanks were all below the detection limit of the ICP-OES).

A second oven-dried filter piece was decalcified overnight in a desiccator with acid fumes that were generated by an open petri dish with concentrated (37%) HCl. The next day, the filters were placed in a fume hood to remove any residual HCl. The C_{org} contents of the filters were

determined with a CN analyser (Fisons Instruments NA 1500). All samples were corrected for filter blanks. The relative standard deviation based on blanks, duplicate filters and in-house standards was generally below 5%.

Particulate inorganic polyphosphate concentrations were quantified according to the method of Martin and Van Mooy (2013). In short, a small filter piece (1 cm^2 ; stored at -80 $^\circ\text{C}$ prior to analysis) was boiled and digested in a 20 mM Tris buffer solution containing RNase, DNase and Proteinase K. After four successive extractions, 4',6-Diamidino-2-phenylindole (DAPI) was added to the final solution. The binding between polyphosphates and DAPI resulted in a peak in the fluorescence emission spectrum of the mixed solution at 550 nm, which was then quantified by a spectrofluorometer (excitation wavelength: 415 nm). The calibration was performed using a polyphosphate standard with a chain length of 45 ± 5 residues (Sigma–Aldrich; S4379), and all concentrations were corrected for blanks. The relative standard deviation based on duplicate filter samples was $<10\%$. As natural polyphosphates may fluoresce more brightly than the synthetic polyphosphate standard, the polyphosphate concentrations are considered to be relative measures and are therefore expressed in nmol equivalents of P per liter (neq L^{-1} ; Martin et al., 2014; Diaz et al., 2016).

2.4. Sequential phosphorus extraction of particulates (Supor)

To investigate the particulate P fractionation in the Black Sea water column, we applied the P extraction scheme method of Ruttenberg (1992) (SEDEX) with modifications by Slomp et al. (1996) as summarized in Table 1, to pieces of the Supor filters (12.5–25% of total filter). The P concentrations in the CDB, MgCl_2 (step 3) and the Na-acetate solutions were determined by ICP-OES whereas all other P concentrations were measured colorimetrically according to the molybdenum blue method (Strickland and Parsons, 1972). The P concentrations were corrected for background concentrations using filter blanks. Standard deviations varied between 0.11 and 0.56 nM for different P fractions (based on duplicate filters).

2.5. Synchrotron-based μXRF and XAS of particles on Isopore filters

The Fe and Mn mineralogy of particles from three water depths (100, 250 and 2000 mbss) was investigated at the beamline BL2-3 at the Stanford Synchrotron Radiation Lightsource (SSRL; Menlo Park, USA). The filters were positioned between Kapton^R tape and mounted on the sample holder. All handling of the water column filters prior to the actual measurements was conducted in an oxygen-free environment to avoid sample oxidation. We performed micron-scale X-ray fluorescence element mapping (μXRF) at 7532 eV with a beam size of 2×2 μm and a step size of 2–5 μm . The intensity counts of the filter from 2000 mbss were multiplied by 0.5 to correct for the longer dwell time (50 ms per pixel versus 25 ms per pixel for the filters from other depths). Elemental maps for Fe

Table 1

The SEDEX scheme according to [Ruttenberg \(1992\)](#), including modifications by [Slomp et al. \(1996\)](#). A H_2O_2 extraction method for organic P was applied to the sediment samples spiked with ^{33}P following [Goldhammer et al. \(2010\)](#) as no combustion oven was available in the isotope lab.

Steps	Extractants	Time	Target phase	Term
1	1M MgCl_2 (pH 8)	0.5 h	Exchangeable P	Ex-P
2	CDB solution (pH 7.6): 0.3M Na_3 citrate; 25 g/L Na dithionite; 1M NaHCO_3	8 h	P bound to Fe oxides and Mn oxides Fe(II)-phosphates ^a $\text{CaCO}_3\text{-P}^{\text{b}}$	CDB-P
3	1M MgCl_2 (pH 8)	0.5 h	Washing step	Authi Ca-P
4	1M Na acetate buffered to pH 4 with acetic acid	6 h	Authigenic apatite	
5	1M MgCl_2 (pH 8)	0.5 h	Washing step	Detr-P
6	1M HCl	24 h	Detrital apatite	
7 (P)	Combustion at 550 °C	2 h	Organic P	Org-P
7 (^{33}P)	1M HCl	24 h	Organic P	Org-P
	20% $\text{H}_2\text{O}_2^{\text{c}}$	48 h		

^a Fe(II)-phosphates such as vivianite can also dissolve in the CDB solution ([Nembrini et al., 1983](#); [Dijkstra et al., 2016](#)).

^b P bound to CaCO_3 can also be extracted in the CDB solution ([Kraal et al., 2017](#)).

^c Remaining H_2O_2 was fumed off in a water bath at 70 °C.

and Mn were plotted on a logarithmic scale in the software package R ([R Core Team, 2016](#)).

Selected spots were investigated with X-ray absorption near-edge spectroscopy (XANES) and extended X-ray absorption fine structure (EXAFS) in the Mn and Fe energy range (6300–6900 eV and 6900–7500 eV, respectively). The monochromator was calibrated against the maximum intensity of the pre-edge feature of potassium permanganate (6543.34 eV) for Mn and the first derivative of the Fe foil (7112 eV) for Fe. We used the ATHENA software package ([Ravel and Newville, 2005](#)) for background subtraction and normalization. We also removed outliers with the deglitching tool and performed a 3-point smoothing on all spectra to reduce overall noise. Individual spectra from different spots that were very similar were merged to obtain average spectra.

The Fe XAS spectra of the reference standards originate from the beamline BL2-3 library ([Kraal et al., 2017](#)). The Mn standards were all characterized by XRD and measured at beamline BM26a (DUBBLE) at the European Synchrotron Radiation Facility (ESRF) in Grenoble, France (beamline layout is described in [Borsboom et al. \(1998\)](#) and [Nikitenko et al. \(2008\)](#)). We evaluated the consistency in the energy calibration by comparing spectra of reference materials that were included in all datasets.

2.6. SEM-EDS analysis of particles on Isopore filters

Particles on carbon-coated Isopore filters were studied in detail at Utrecht University with a scanning electron microscope (FEI Helios NanoLab G3 UC). We performed elemental mapping with an acceleration voltage of 15 kV in 0.6 by 0.6 μm steps (dwell time = 3 μs ; energy range = 20 keV). The total area analysed per filter was ~ 600 by 400 μm . Within this filter area, particles were selected for SEM imaging and more detailed elemental mapping (step size of $\sim 0.03 \mu\text{m}$). The relative abundances of elements on the particles were estimated using the AZtec software

(excluding carbon, oxygen, sodium and chloride for calculations). The 100 mbss filter was also investigated using a HyperProbe electron probe microanalyzer ([Appendix B](#)).

2.7. ^{210}Pb analysis, mass accumulation rates and burial efficiencies

Freeze-dried and ground samples from the 0–10 cm sediment interval at station 2 (6 samples) were used for ^{210}Pb (half-life 22.3 y) analysis using a Canberra BeGe gamma-ray spectrometer. The activities of ^{210}Pb and other γ -emitting radionuclides were determined using γ spectrometry. Each sample was measured until at least 200–250 ^{210}Pb gamma-ray counts were recorded. After correction of the ^{210}Pb activity for background (supported) ^{210}Pb activity, the constant flux model ([Sanchez-Cabeza and Ruiz-Fernández, 2012](#)) was used to calculate mass accumulation rates (MAR, $\text{g cm}^{-2} \text{y}^{-1}$). Sedimentation rates (SR, cm y^{-1}) were obtained by dividing the MAR by the dry bulk density (g cm^{-3}).

Deposition and burial rates and burial efficiencies for P and C_{org} at station 2 were calculated as detailed below. Burial rates of the various forms of P and C_{org} were obtained by multiplying the MAR with the P and C_{org} concentrations for the depth interval of 2–3 cm ([Table 2](#)), assuming that most change in concentration due to organic matter degradation occurs in the upper 2 cm of the sediment ([Sun and Wakeham, 1994](#)). Diffusive PO_4 fluxes across the sediment-water interface were determined using Fick's law of diffusion and PO_4 porewater profiles and bottom water concentrations obtained during the 2013 and 2015 cruises ([Appendix C](#)). The rate of deposition of total P was calculated as the sum of the burial flux of total P and the diffusive flux of PO_4 across the sediment-water interface ([Jensen et al., 1995](#)).

The SEDEX extraction scheme ([Table 1](#)) was applied to sediments from 2 to 3 cm depth to distinguish between different P forms: detrital P, exchangeable P,

Table 2

Burial rates, deposition rates and burial efficiencies of phosphorus (P) and organic carbon (C_{org}). The P and C_{org} concentrations in the sediment interval from 2 to 3 cm depth at station 2 are from Kraal et al. (2017). The SEDEX method of Ruttenberg (1992) as modified by Slomp et al. (1996) extracted various P fractions: detrital P, exchangeable P, CDB-extractable P, authigenic Ca-P, and organic P (reactive P is total P minus detrital P). The deposition rate of C_{org} was calculated assuming the Redfield C:P ratio for organic matter (106:1 mol mol⁻¹) and using the C_{org} :P ratio of particles from 2000 mbss (288:1 mol mol⁻¹; Fig. 2). Burial efficiencies were calculated as the percentage of the incoming depositional flux that was buried below a depth of 2 cm.

Station 2	Concentration ($\mu\text{mol g}^{-1}$)	Burial rate ($\mu\text{mol m}^{-2} \text{y}^{-1}$)	Deposition rate ($\mu\text{mol m}^{-2} \text{y}^{-1}$)	Burial efficiencies (%)
Total P	18.3	1098	4018	27
Detrital P	1.5	90	90	100
Exchangeable P	1.1	66	0–66	0–100
CDB-extractable P	4.5	270	0–270	0–100
Authigenic Ca-P	2.3 (0.8) ^a	138	0–48	0–288 ^b
Organic P	8.9	534	3544–3928	14–15
Reactive P	16.8	1008	3928	26
Organic C (C_{org} :P = 106)	6260	375,600	425,908	88
Organic C (C_{org} :P = 288)	6260	375,600	1,157,184	32

^a Authigenic Ca-P concentration in the top 0.5 cm of sediments.

^b Including Ca-P formation in the sediment (authigenesis), so >100%.

citrate-dithionite-bicarbonate (CDB)-extractable P, authigenic Ca-P and organic P. Detrital P is an unreactive P phase in the water column and sediments, therefore the deposition rate was assumed equal to the burial rate. The maximum deposition rate of exchangeable and CDB-extractable P was considered to be similar to the burial rate (assuming no *in-situ* formation of CDB-extractable P). Authigenic Ca-P is low in the top 0.5 cm of sediment (0.8 $\mu\text{mol g}^{-1}$) and gradually increases with depth (2.3 $\mu\text{mol g}^{-1}$), suggesting apatite formation in the surface sediments (Kraal et al., 2017). The maximum deposition rate of authigenic Ca-P was assumed equal to the MAR multiplied by the authigenic Ca-P concentration in the top 0.5 cm of the sediment. If we assume that only P released from organic P is responsible for the diffusive PO_4 out of the sediments, then the rate of organic P deposition should be equal to the deposition rate of total P minus that of all inorganic P. Maximum rates of organic P deposition were calculated assuming that detrital P was the only source of inorganic P, and minimum rates of organic P were calculated assuming maximum deposition rates for all inorganic P phases. Deposition rates of C_{org} were calculated from the organic P deposition rate assuming a Redfield C:P ratio of 106:1 mol mol⁻¹ for marine organic matter, and in addition by assuming a C_{org} :P ratio similar to our estimation of the particulate C_{org} :P ratio at 2000 mbss. The burial efficiency, i.e. the percentage of the depositional flux of P that is buried (e.g. Jensen et al., 1995) was calculated for all P forms and organic C. We also calculated the burial efficiency for reactive P (total P minus detrital P).

2.8. Synchrotron-based μXRF and XAS of resin-embedded sediments

We embedded a small subsample (~ 1 cm diameter) of the top 0–7 cm of a multicore in resin under anoxic conditions according to the method of Jilbert and Slomp (2013)

for a detailed investigation of Ca, Fe, Mn and P enrichments in the surface sediment. The top section of the resin-embedded mini-core was analysed at the beamline BL2-3 at the Stanford Synchrotron Radiation Light source (Menlo Park, USA). Elemental μXRF mapping was performed at 7532 eV with a beam size of $2 \times 2 \mu\text{m}$ and a step size of $5 \times 5 \mu\text{m}$. Enrichments in Mn at the sediment-water interface were investigated by Mn XANES (6300–6900 eV; see Section 2.4 for technical details).

2.9. ^{33}P incubation experiments

To investigate the conversion of dissolved PO_4 in the surface sediments to solid-phase P, a ^{33}P tracer experiment was performed with surface sediment from stations 2 and 9. We sampled the first 7 cm of sediment at station 2 to obtain enough sediment for our incubation. At station 9, we sampled the oxidized layer of surface sediment (~ 0 –1 cm). Seawater from the deepest CTD deployment at each station was spiked with a ^{33}P radiolabel solution ($\text{H}_3^{33}\text{PO}_4$; Perkin Elmer; half-life of 25.4 days) and mixed with the surface sediment in a 1:1 volume ratio. The sediment slurry was divided among centrifuge tubes, resulting in an initial radioactivity in each sample of 10–40 kBq ^{33}P . The added $^{33}\text{PO}_4$ content was negligible compared to the PO_4 concentrations in the sediment slurries so that the radionuclide functioned as a true tracer (<1%). Handling of samples from station 2 was conducted in an oxygen-free environment to avoid oxidation artifacts. Slurry samples with 3.7% formaldehyde served as abiotic controls and were treated in the same way as the other samples.

The ^{33}P -spiked samples were incubated for 0, 3–5 or 30 days on a shaker table at 9 °C in the dark and stored at -80 °C until analysis. At the end of the experiment, all samples were thawed and directly centrifuged to separate the overlying water from the sediments. The radioactivity in the overlying water was measured in scintillation vials

with an Ultima Gold XR scintillation cocktail (Perkin Elmer) on a Tri-carb 2300 TR scintillation analyser (Packard Instrument Company, LaGrange, IL, USA). Total activity in the aqueous phase of the incubated slurries was obtained by multiplying the activity in the overlying water by the total volume of water in the sample. After three washes with ultraclean water, the residual sediment was subjected to the SEDEX method of Ruttenberg (1992) with modifications by Slomp et al. (1996) and Goldhammer et al. (2010) (Table 1). The radioactivity in the SEDEX extracts was multiplied by the extraction volume to obtain the total sediment activity. Regarding the station 9 sediments, we used a correction factor of 1/0.45 as we only applied the SEDEX procedure to a subsample of the ^{33}P -spiked sediments (45% of total sample mass). Organic-bound P in the ^{33}P -spiked sediments was targeted using a 20% hydrogen peroxide solution (H_2O_2) at room temperature for 48 h (Table 1). Oxidation of organic matter led to high pressure build-up and subsequent overflow of SEDEX solutions out of centrifuge tubes in some of the samples from station 2. The results from these samples were discarded. A subsample of each SEDEX extract was mixed with a scintillation cocktail (Ultima Gold XR) and immediately analysed with the Tri-carb 2300 TR scintillation analyser. We used SEDEX solutions with known ^{33}P activity to correct for chemical quenching and the samples were corrected for background radioactivity using blanks. All activities were back-calculated to the start of the experiment assuming exponential decay. The first six steps of the SEDEX were conducted in an oxygen-free environment to avoid sample oxidation and associated changes in P fractionation. All experiments were performed in triplicate. Differences in mean activities between the sample groups (time steps and normal/abiotic control) were compared by one-way analysis of variance (ANOVA) with post hoc Tukey tests in Sigmaplot 12.3. Methods and results of ^{33}P radiotracer incubations with additional shelf edge sediments (43°42.6' N–30°06.1' E) are included in Appendix D.

The P distribution in non-radioactive mixed surface sediments from stations 2 and 9 was also investigated with SEDEX (Table 2). The extraction scheme was also applied to synthesized carbonated hydroxyapatite to assess its solubility in the CDB-extraction step (Appendix E). The P concentration in the CDB extracts were measured by ICP-OES. All other P concentrations were determined with the molybdenum blue method (Strickland and Parsons, 1972).

3. RESULTS

3.1. Trends in solutes and particles with water depth

The water column at station 2 is density-stratified with a sharp increase in density and salinity between 40 and 200 m to values of 16.7 σ_θ (sigma theta, kg m^{-3}) and 21.5, respectively (Fig. 1). Due to the circulation patterns in the Black Sea, characteristic features in the redoxcline tend to occur at greater depth in the shelf areas compared to the central gyres. Plotting trends as a function of density instead of water depth is therefore preferred (Murray and Yakushev, 2006). The temperature profile shows a distinct trend with

the lowest temperature at a density of 15.1 σ_θ (50 m water depth) and higher values in the deeper water column ($\sim 8.8^\circ\text{C}$).

The redoxcline at station 2 is situated between 80 and 110 mbss (15.9–16.3 σ_θ ; Fig. 2). Oxygen concentrations fall below 0.5 μM underneath the upper limit of the redoxcline. Below the redoxcline, HS^- concentrations gradually increase to a maximum value of 420 μM at 2000 mbss (17.2 σ_θ). The depth profile of dissolved PO_4 displays a minimum at the top of the redoxcline (0.6 μM), a maximum in the lower part of the redoxcline (7.9 μM) and a broad minimum to values as low as 5 μM at 170 mbss. Particulate P concentrations are elevated in the oxic waters (55 nM), very high within the redoxcline at 90 mbss (113 nM; 16.0 σ_θ) and low (~ 10 nM) in the sulfidic waters. Dissolved Mn concentrations are below detection in the oxic waters, increase within the redoxcline, reach values of almost 8 μM just below the redoxcline and then decrease with water depth. The redoxcline at 95 mbss is enriched in particulate Mn (85 nM; 16.1 σ_θ) whereas the sulfidic deep waters do not contain particulate Mn (< 1 nM). A maximum in dissolved Fe of 0.32 μM is observed in the sulfidic water at 170 mbss (16.6 σ_θ), just below the maximum in dissolved Mn. We observe three maxima in particulate Fe: at 85 mbss (25 nM; 16.0 σ_θ), 250 mbss (41 nM; 16.8 σ_θ) and 2000 mbss (27 nM; 17.2 σ_θ). The highest concentrations of particulate C_{org} were observed at 50 mbss (15.1 σ_θ) and at 2000 mbss (17.2 σ_θ). Particulate molar $\text{C}_{\text{org}}:\text{P}$ ratios were close to the Redfield ratio for marine organic matter (106:1 mol mol^{-1}) at all depths, except for the redoxcline ($\text{C}_{\text{org}}:\text{P}$ ratios $< 30:1$ mol mol^{-1}) and the water column at 2000 mbss (288:1 mol mol^{-1}). The trend in polyphosphates generally follows the trend in particulate P with a maximum at a density of 16.0 σ_θ (90 mbss; 0.92 neq L^{-1}). The ratio between polyphosphates and particulate P is below 0.1 eq mol^{-1} at all water depths.

3.2. Particulate P fractions with water depth

Exchangeable and CDB-extractable P are the main particulate P phases in the oxic waters (> 15.2 σ_θ ; Fig. 3). The particulate P enrichment in the upper zone of the redoxcline (15.9 σ_θ ; 95 mbss) mainly consists of CDB-extractable P (45 nM) and exchangeable P (12 nM). In the lower part of the redoxcline and the deeper sulfidic waters CDB-extractable and exchangeable P together account for ~ 4 nM of particulate P. Particulate organic P is only a minor fraction in the oxic waters and the upper part of the redoxcline (< 0.5 nM). Particulate organic P concentrations increase from the lower boundary of the redoxcline to the sulfidic deep waters, with values up to 3.9 nM at 2000 mbss (17.2 σ_θ). Authigenic Ca-P minerals and detrital P only represent a small fraction of the particulate P pool throughout the water column.

3.3. Examination of Fe and Mn particles by XAS

The mineralogy of Fe and Mn particles from 100, 250 and 2000 mbss (16.1, 16.8 and 17.2 σ_θ , respectively) on 0.2 μm Isopore filters was investigated by synchrotron-

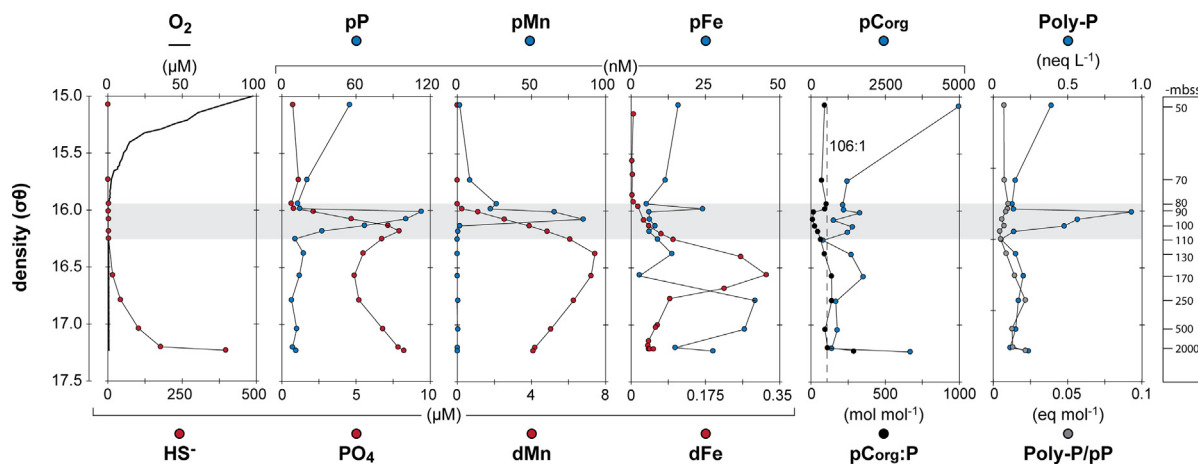


Fig. 2. Depth trends in concentrations of particles and dissolved constituents at station 2 (dMn: dissolved Mn; dFe: dissolved Fe). Actual water depth is given in meters below sea surface (mbss). Particulate P (pP), Mn (pMn), Fe (pFe), organic carbon (C_{org}), C_{org}:P ratios (pC_{org}/P) and inorganic polyphosphate concentrations (Poly-P) were determined using GFF filters collected in 2013 (in-situ pumps).

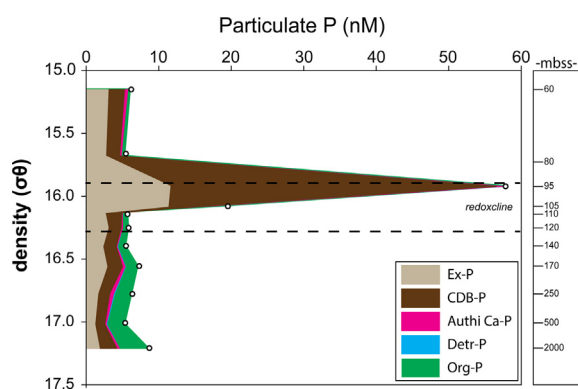


Fig. 3. Trends in particulate phosphorus fractions with density at station 2. Actual water depth is given in meters below sea surface (mbss). The dotted lines indicate the position of the redoxcline and the open circles show densities at which samples were taken (with associated depth in the right box). We applied the SEDEX protocol of Ruttenberg (1992) with modifications as described in Table 1 to particulates collected on Supor filters in September 2015. The fractions are exchangeable P (Ex-P), CDB-extractable P (CDB-P), authigenic Ca-P minerals (Authi Ca-P), detrital P (Detr-P) and organic P (Org-P).

based μ XRF (Fig. 4) and XAS (Fig. 5). The water column at 100 mbss contains Fe-rich, Mn-rich and mixed Fe-Mn particles. Note that the 0.7 μ m GFF filters from 100 mbss water depth were depleted in particulate Mn at this depth (<2 nM; Fig. 2). This difference in Mn content between both filters may be due to a slight change in the position of the redoxcline between both deployments. The filters from the sulfidic water column contain Fe particles but were depleted in Mn particles (Fig. 4).

All water column Fe particles from 100 mbss and some particles in the deeper water column (250 and 2000 mbss) are characterized by pre-edge and white line positions that are typical for Fe(III)-phases (Fig. 5A). The Fe XANES spectrum of the particles does not contain the pre-edge shoulder of magnetite. Due to high signal-to-noise ratios

of the Fe EXAFS spectra, we could not distinguish between clay-associated Fe(III) and other Fe oxides in our sample spectra based on linear combination fitting using Fe reference spectra (Fig. 5B). Fe(III) XANES and EXAFS spectra show little change with water depth, implying a similar Fe (III) mineralogy. In addition to Fe(III) particles, the sulfidic waters also contained particles with Fe XANES and EXAFS spectra that closely resemble the spectrum of pyrite (FeS₂).

The XANES spectrum of the Mn-particles at 100 mbss resembles the spectrum of birnessite, a mixed Mn(III/IV) oxide, and not that of the Mn(II) and Mn(III) reference materials MnO and bixbyite, respectively. (Fig. 5C). The Mn EXAFS spectrum of the water column particles is also most similar to the spectrum of birnessite (Fig. 5D).

3.4. Elemental composition of individual particles by SEM-EDS

Individual particles from 100, 250 and 2000 mbss were investigated by SEM-EDS (Fig. 6). On the filter from 100 mbss, we observed Fe and Mn particles containing P that were <10 μ m in size (Fig. 6A and B). The mixed Fe and Mn phases were either enriched in Mn or in Fe (Appendix B). The filter also contained larger agglomerates that presumably consist of a mixture of Mn oxides with P, salts, clays and organic matter (including silica(Si)-rich debris of diatoms; Fig. 6C and D). We also observed CaCO₃-rich exoskeletons of coccolithophores (Fig. 6A).

The 250 mbss filter contained agglomerates of pyrite, organics, clays and salts (Fig. 6E-G). The P-rich particles in Fig. 6F are assumed to be organic with attached Mg from salt as inorganic precipitation of Mg-phosphates in modern marine environments is considered impossible (Golubev et al., 2001). Note, that the high background carbon on the carbon-coated filters precludes identification of organic particles by SEM-EDS based on carbon contents. We further detected an Fe particle (Fig. 6G) and apatite (Fig. 6H). Similar to the 250 mbss filter, the filter from

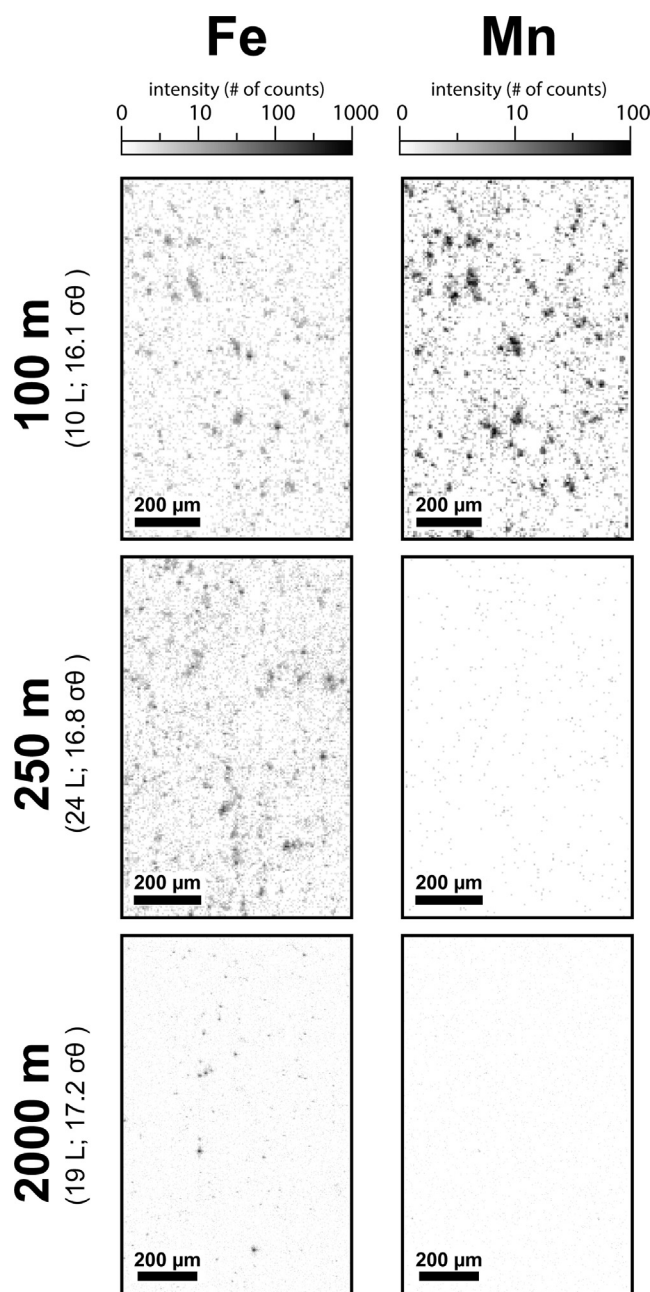


Fig. 4. Fe and Mn μ XRF maps of particles collected on Isopore filters (0.2 μ m) for water depths of 100, 250 and 2000 mbss. The intensity (# of counts) is given on a logarithmic scale. The volume of filtered water and the density for each water depth are given between brackets.

2000 mbss contained clay particles (high in Si, K, Al and Fe) with some P (Fig. 6I). We further identified a Fe particle with P and Si (Fig. 6J). The P enrichment on the Fe particle results in a clear correlation between Fe and P counts (Fig. 6K). Counts for Mn were very low on the filters with particles from 250 and 2000 mbss, as illustrated for 2000 mbss in Fig. 6L.

3.5. Rate of deposition and burial efficiency

Sedimentation rates (SRs) and mass accumulation rates (MARs) in the upper cm of sediment at station 2 are 0.23

cm y^{-1} and $\sim 60 \text{ g m}^{-2} \text{ y}^{-1}$ (Fig. 7), which is in agreement with other estimates for the western Black Sea basin (Crusius and Anderson, 1992). The burial rate of total P in the sediments at station 2 is $1098 \mu\text{mol g}^{-1}$ (Table 2) and the average diffusive flux of PO_4 at station 2 is $2920 \mu\text{mol m}^{-2} \text{ y}^{-1}$ (based on porewater PO_4 profiles for 2013 and 2015; Appendix C). The deposition rate of total P is then estimated to be $4018 \mu\text{mol m}^{-2} \text{ y}^{-1}$. This results in a burial efficiency for total P of 27%. Organic P is the major burial P pool in the sediments (49% of total P) and is also the main depositional P phase. The maximum deposition rate of exchangeable and CDB-extractable P is 66 and

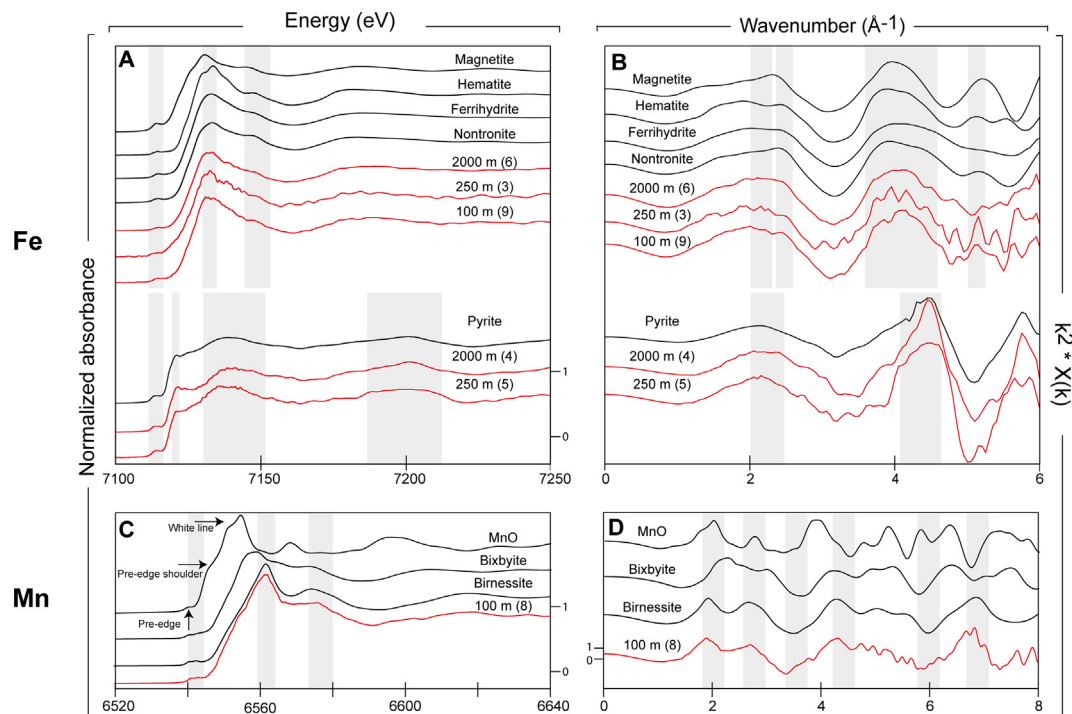


Fig. 5. Fe and Mn XANES and EXAFS spectra for water column particles from water depths of 100, 250 or 2000 mbss (red) and various standards (black). The grey shades highlight areas with characteristic features within the spectra. We merged 2–9 individual spectra from different spots that were very similar to obtain average spectra (number of individual spectra per merged spectrum is given between brackets). The particles were collected on Isopore filters (0.2 μm). Black arrows show main features of the MnO XANES spectrum. The pre-edge feature and white line (main absorption step) are also observed in all other Fe and Mn XAS spectra in the figure. (For interpretation of the references to colour in this figure legend, the reader is referred to the web version of this article.)

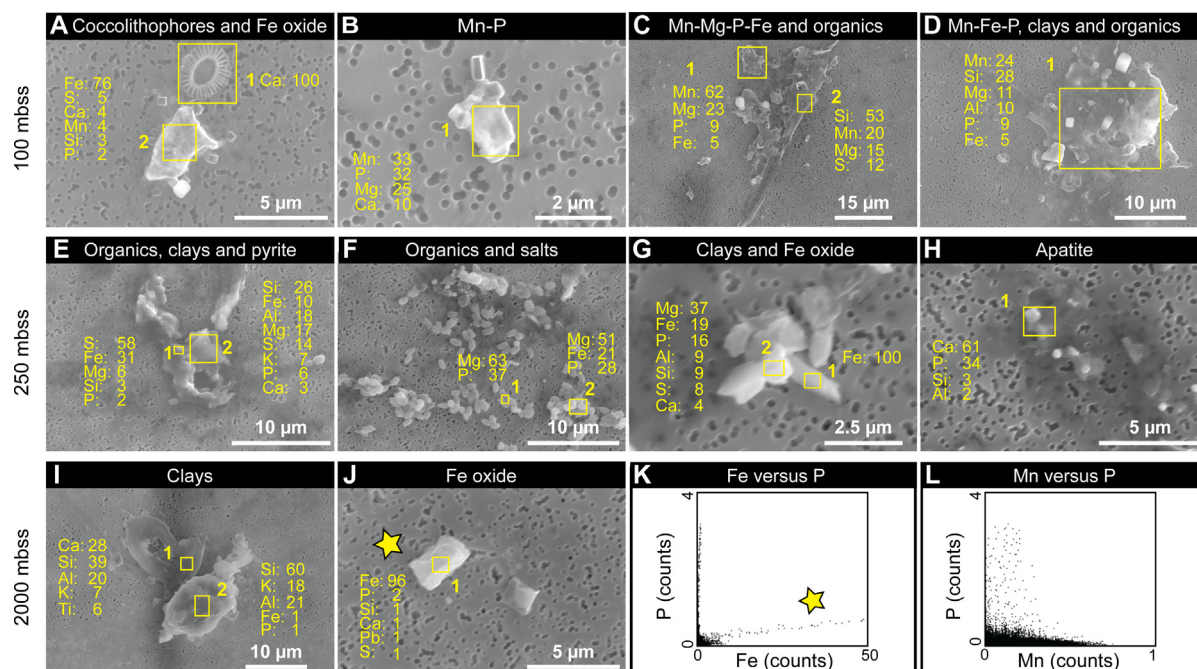


Fig. 6. SEM images with EDS results of particles from water depths of 100, 250 and 2000 mbss (A–J) and correlation plots for Fe–P and Mn–P from 2000 mbss (K and L). Particles were collected on Isopore filters (0.2 μm). The elemental composition in mol% was estimated with AZtec software and excludes carbon, oxygen, sodium and chloride (manually inserted in the figures). The Fe oxide particulate from 2000 mbss, indicated with a yellow star, contains P (J and K).

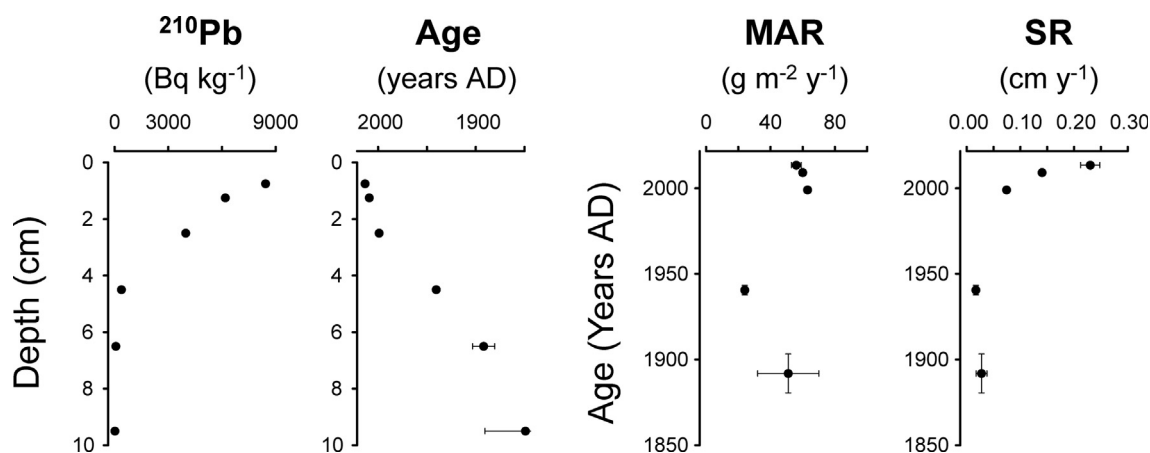


Fig. 7. Depth profiles of ^{210}Pb and sediment age at station 2 and corresponding mass accumulation rates (MAR) and sedimentation rates (SR) as a function of sediment age. The ^{210}Pb activity was corrected for background (supported) ^{210}Pb activity. The mass accumulation rates were calculated using the constant flux model (Sanchez-Cabeza and Ruiz-Fernández, 2012). Error bars show standard deviations.

270 $\mu\text{mol m}^{-2} \text{y}^{-1}$, respectively. Only a minor fraction of particulate P may also settle onto the seafloor as detrital P (90 $\mu\text{mol m}^{-2} \text{y}^{-1}$) and authigenic Ca-P (max. 48 $\mu\text{mol m}^{-2} \text{y}^{-1}$). The burial efficiency of organic P ranges from 14 to 15% and thus is much lower than the C_{org} burial efficiency of 88% when assuming that the $C_{\text{org}}:\text{P}$ ratio of incoming organic matter is similar to the Redfield ratio of 106:1 mol mol $^{-1}$.

3.6. Elemental distribution in the surface sediments

The elemental maps for the upper cm of the sediment at station 2 show a clear correlation between P and Ca (Fig. 8). Sediments at the sediment-water interface contain some Mn. Their Mn XANES spectrum is similar to the Mn XANES spectrum of rhodochrosite (MnCO_3). Enrichments of Fe are mainly observed where P and Ca are low.

3.7. ^{33}P incubation experiments

We were able to track most of the added ^{33}P activity in either the solid or aqueous phase of the slurries from station 2 and 9 (Table 3). The remaining ^{33}P activity was likely lost during washing of the slurries with ultraclean water prior to the P extraction scheme. More than 70% of all ^{33}P activity

was directly incorporated in the solid phase (day 0 = within a few hours) for both stations. The ^{33}P activity in the aqueous phase continued to decrease with time in the station 2 samples, resulting in minimum ^{33}P activities in the aqueous phase on day 30. At station 2, the solid-phase ^{33}P activity was significantly higher on day 30 than at the start of the experiment (day 0). No statistical differences between the samples and abiotic control group were observed.

CDB-extractable P is the major P pool in the mixed sediments from station 9, while authigenic Ca-P, CDB-extractable P and organic P are all major P pools in the mixed sediments from station 2 (Fig. 9; grey dotted lines and numbers below the x-axis). At both stations, highest ^{33}P activities were observed in the P fraction that was extracted in the CDB solution of the SEDEX (>80%). This uptake was not biologically controlled as the ^{33}P activity in the CDB fraction was similar between the sediment slurries treated with formaldehyde (abiotic control) and the untreated sediment slurries. There was a significant decrease in the ^{33}P activity in the exchangeable P fraction with time at both stations. At station 9, the ^{33}P activity in the organic P fraction was significantly higher after 30 days than at the start of the incubation (day 0; $p < 0.01$). We only observe significant differences between the samples and abiotic control group at station 9, with the abiotic

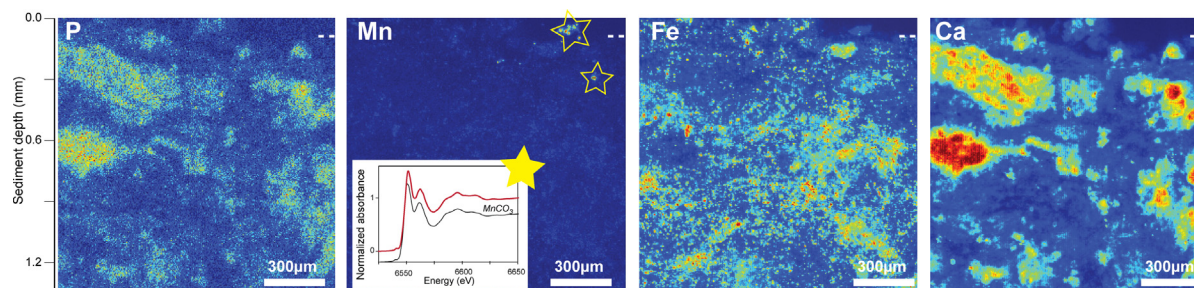


Fig. 8. Synchrotron-based μXRF maps of phosphorus (P), manganese (Mn), iron (Fe) and calcium (Ca) and Mn-XANES for Mn enrichments near the sediment-water interface (SWI) at station 2. On the left side of the map, the SWI is located at the top of the elemental map. The dashed line indicates the position of the SWI at the right side of the elemental map. Average spectrum of the Mn-enrichments (yellow star; # of spectra = 2) is similar to the Mn-XANES spectrum of rhodochrosite (MnCO_3).

Table 3

^{33}P budget as % recovery of ^{33}P activity added at the start of the experiment. Standard deviation based on triplicates is indicated between brackets (control = abiotic control). Differences in small letters between groups (a/b) indicate statistical differences in means between the time steps, as determined by one-way ANOVA tests ($p < 0.01$). For example, the ^{33}P in the aqueous phase at station 9 at the start (0 days) was significantly different from the ^{33}P concentration at day 3 and 30 (a versus b), whereas the differences between day 3 and 30 were not significant (same letter b).

	^{33}P in solid phase (%)	^{33}P in aqueous phase (%)	Total ^{33}P (%)
St. 9 (days)			
0	83.7 (6.4)	1.2 (0.03) ^a	84.8 (6.4)
3	79.5 (16.4)	0.6 (0.2) ^b	80.1 (16.5)
30	75.7 (3.7)	0.7 (0.07) ^b	76.4 (3.7)
0 control	84.8 (7.2)	0.9 (0.1)	86.7 (7.3)
3 control	75.2 (7.8)	0.9 (0.2)	76.1 (7.9)
30 control	72.5 (2.5)	0.8 (0.02)	73.3 (2.4)
St. 2 (days)			
0	70.7 (2.2) ^a	19.9 (3.4)	90.5 (5.6)
5	76.7 (2.8)	12.9 (2.1)	89.6 (1.3)
30	80.6 (3.5) ^b	7.5 (0.7)	88.1 (4.0)
0 control	73.2 (0.9)	20.9 (2.9)	94.1 (2.4)
5 control	80.3 (2.8)	8.7 (1.6)	89.0 (1.3)
30 control	89.1 (2.6)	3.8 (0.07)	92.9 (2.6)

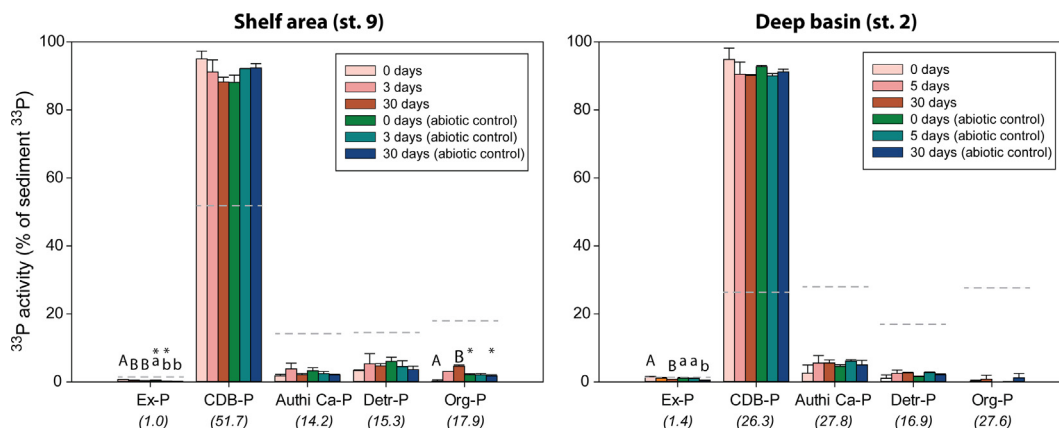


Fig. 9. Distribution of ^{33}P activity in the sedimentary P fractions for station 9 and 2. The dashed grey lines show relative P content in the sediment slurries (actual values are given between brackets on the x-axes). We applied the SEDEX protocol of [Ruttenberg \(1992\)](#) with modifications as described in [Table 1](#). Different alphabetical superscripts (a/b) indicate statistical differences in means between the time steps as determined by one-way ANOVA tests ($p < 0.01$; small letters for samples and capital letters for abiotic control set). Asterisks show significant differences in means between the sample and abiotic control group from same fraction and time step (one-way ANOVA tests; $p < 0.01$).

samples having lower ^{33}P activities in the exchangeable and organic ^{33}P than the samples that were not treated with 3.7% formaldehyde ([Appendix E](#)). In addition to the ^{33}P radiotracer experiment, we show that roughly 30% of synthesized carbonated hydroxyapatite dissolves in the CDB extraction step ([Appendix F](#)).

4. DISCUSSION

4.1. Organic matter is a major carrier of P towards the seafloor

The Black Sea surface waters are inhabited by a diverse community of phytoplankton, consisting primarily of diatoms, dinoflagellates and coccolithophores ([Oguz and](#)

[Merico, 2006](#)). Together, these micro-organisms are estimated to be responsible for the fixation of $\sim 8300 \text{ mmol C m}^{-2} \text{ y}^{-1}$ in the surface waters ([Deuser, 1971](#)). Assuming a C:P ratio for marine organic matter of $106:1 \text{ mol mol}^{-1}$ ([Redfield, 1958](#)), this results in the simultaneous fixation of $78 \text{ mmol P m}^{-2} \text{ y}^{-1}$. Most of the organic matter is degraded in the surface waters ([Deuser, 1971](#)). This is in accordance with the observed decrease in C_{org} and particulate P in the oxic waters at our study site ([Fig. 2](#)). Besides phototrophic production in surface waters, 10–30% of the total carbon fixation in the Black Sea water column may occur just below the redoxcline via chemosynthesis ([Jørgensen et al., 1991](#); [Sorokin et al., 1995](#); [Yilmaz et al., 2006](#); [Wakeham et al., 2007](#)). This carbon fixation pathway can explain the small increase in C_{org} concentration in the

upper sulfidic waters between a density of 16.3 and 16.7 $\delta\theta$ at our site (Fig. 2). A similar C_{org} increase in the upper sulfidic waters was observed previously in the central deep basin (Wakeham et al., 2007). Yearly ca. 4000 $\mu\text{mol P m}^{-2}$ is estimated to be deposited onto the seafloor (Table 2). If we attribute all upward diffusing PO_4 to organic matter degradation and associated P release, then at least 85% is estimated to be deposited as organic P (Table 2; Appendix C).

Our P fractionation results show that organic P is only a minor particulate P phase in the oxic waters (Fig. 3). This particulate organic P fraction does increase in the sulfidic waters, perhaps due to fixation of dissolved PO_4 via chemosynthesis. Still, particulate organic P at 2000 mbss only accounts for 43% of the total particulate P pool, and thus is not in accordance with our estimated flux of organic P towards the seafloor ($>85\%$ of the total P pool). These discrepancies might be caused by the large seasonal variability in the particulate organic matter flux towards the seafloor (Hay et al., 1990). Seasonal variation may also explain the difference between total extracted particulate P determined as the sum of SEDEX P phases (September 2015; Fig. 3) and total particulate P (June 2013; Fig. 2).

If settling organic matter has a $C_{org}:P$ ratio similar to the Redfield ratio for organic matter (106:1 mol mol^{-1}), then the depositional flux of organic carbon towards the seafloor in the deep basin is $\sim 426 \text{ mmol m}^{-2} \text{ y}^{-1}$ (Table 2). This is close to estimated C_{org} fluxes in sulfidic waters (1200 mbss) in the southern Black Sea based on to sediment traps (110–400 $\text{mmol m}^{-2} \text{ y}^{-1}$ Hay et al., 1990). This organic matter deposition rate will, however, result in a C_{org} burial efficiency in the underlying sediments that is higher than values earlier reported for the deep basin of the Black Sea and other euxinic systems (88% versus 13–80%; Table 2; Canfield, 1989; Slomp et al., 2002). We therefore hypothesize that preferential release of P relative to C from organic matter (Ingall et al., 1993) due to the activity of carbon-limited bacteria in the sulfidic deep waters (Steenbergh et al., 2011, 2013), may result in higher $C_{org}:P$ ratios in settling organic matter than 106:1 mol mol^{-1} . This is also suggested by our particulate $C_{org}:P$ trend in the water column (Fig. 2) and is in accordance with the redox-dependence of $C_{org}:P$ ratios observed in marine sediments (Algeo and Ingall, 2007). Whereas the particulate $C_{org}:P$ ratio in the upper part of the sulfidic water column (110–1000 mbss) is close to 106:1 mol mol^{-1} , the $C_{org}:P$ ratio at 2000 mbss is considerably higher (288:1 mol mol^{-1} ; Fig. 2). Applying a $C_{org}:P$ ratio of 288:1 mol mol^{-1} for settling organic matter results in a C_{org} deposition rate of 1157 $\text{mmol C m}^{-2} \text{ y}^{-1}$ and an organic carbon burial efficiency of 32% (Table 2). Although we cannot determine how representative this single measurement is for the mean $C_{org}:P$ ratio of particles deposited onto the seafloor, this calculation illustrates that it is likely that particles settling onto the deep basin seafloor have a $C_{org}:P$ ratio which is higher than 106:1 mol mol^{-1} . Preferential release of P from organic matter may have continued after deposition, resulting in a low burial efficiency of organic P relative to C_{org} in the surface sediments (14–15% versus $>32\%$; Table 2). The elevated $C_{org}:P_{org}$ ratio of 702 mol mol^{-1} in the sediments at 2–3 cm depth is indicative for ongoing preferential release

of P relative to organic C from organic matter during early diagenesis (Table 2). The sulfidic conditions in both the deep waters and surface sediments in the Black Sea thus result in less organic P burial in the sediments than expected based on C_{org} deposition rates.

4.2. Inorganic P particles in the redoxcline

Euxinic basins are enriched in inorganic P particles in or close to the redoxcline (Dellwig et al., 2010; Diaz et al., 2012; McParland et al., 2015). In the Black Sea, the presence of these inorganic P particles results in a particulate P maximum of $>80 \text{ nM}$ (Fig. 2; e.g. Coban-Yildiz et al., 2000), as well as low particulate $C_{org}:P$ ratios ($<25:1 \text{ mol mol}^{-1}$; Fig. 2). Long-chain inorganic polyphosphates (≥ 15 P atoms) can be an important P pool in marine redoxclines (Diaz et al., 2012) but at our site inorganic polyphosphate concentrations were very low ($<1 \text{ neq L}^{-1}$ at all depths; Fig. 2). In contrast to inorganic polyphosphates, Mn-Fe-P particles are abundant in the redoxcline at station 2 (100 mbss). This is demonstrated by synchrotron-based μXRF and XAS, providing evidence for the presence of mixed Mn(IV)- and Fe(III)-rich particles (Figs. 4 and 5), and SEM-EDS analyses, which showed that Mn and Fe particles contain P (Fig. 6A–D). At our site, most of the mixed Fe-Mn particles were enriched either in Mn or in Fe (Fig. 6 and Appendix B). The presence of these Mn-Fe-P particulates results in a large pool of particulate exchangeable and CDB-extractable P in the redoxcline (Fig. 3).

The 100 mbss Mn(IV)-rich particles have molar Mn:P ratios between 1:1 and 7:1 (Fig. 6; based on EDS counts). These values are close to the previously reported mean Mn:P ratio of Mn(IV)-P particles in the Black Sea redoxcline of 2.6:1 mol mol^{-1} (Dellwig et al., 2010). Colloidal Mn(III)-P and perhaps some Mn(IV)-P may also be collected as particulate Mn on our 0.2 μm Isopore filters and 0.7 μm GFF filters while being too small for identification by synchrotron-based XAS and SEM-EDS. Our particulate P maximum is indeed located at a density of 16.0 $\delta\theta$ where Mn(III) is assumed to be at a maximum (Fig. 2; Trouwborst et al., 2006). With a molar Mn:P ratio of 0.17:1 or 0.25:1, Mn(III)-complexes with pyrophosphate (simplified as Mn(III)-P) are a more efficient carrier of P in the water column than Mn(IV)-P (Davies, 1969; Yakushev et al., 2009). The Mn(III)-P concentrations in the Black Sea redoxcline can be as high as $\sim 50 \text{ nM}$ (based on pyrophosphate measurements; Pakhomova et al., 2009; Yakushev et al., 2009). These P phases might thus explain a large fraction of the particulate P pool in the upper part of the redoxcline. The maximum concentration of particulate Fe in the redoxcline is lower than the maximum concentration of particulate Mn (25 versus 80 nM ; Fig. 2). When we assume a molar Fe:P ratio of 2:1, as reported in Dellwig et al. (2010), Fe(III)-P phases only represent $\sim 5\%$ of the particulate P in the redoxcline. In reality, this percentage is likely even smaller as this calculation does not account for the Fe fraction in clays and the presence of almost pure Fe oxides without abundant P (as in Fig. 6A).

Note that our observed Mn-Fe-P dynamics in the redoxcline, with a major role for Mn and not for Fe, may not be a universal signature for the deep basin as there is a large range in maximum particulate Mn and Fe concentrations in the Black Sea redoxcline (8–2300 nM and 15–300 nM, respectively; [Lewis and Landing, 1991](#); [Pakhomova et al., 2009](#)). This variation is proposed to be linked to spatial differences in lateral inputs of Mn and Fe and seasonal variability ([Pakhomova et al., 2009](#)). Storms may, for instance, transport relatively large amounts of oxygen towards the redoxcline, which in turn affects oxidation and reduction reactions and, subsequently, the redoxcline dynamics of Mn, Fe and P.

4.3. Fate of Mn-P and Fe-P in sulfidic deep waters

Whereas most studies on Mn-Fe-P dynamics in euxinic basins focus on the particulate dynamics in or close to the redoxcline (e.g. [Dellwig et al., 2010](#); [Yakushev et al., 2009](#)), we specifically wish to address the fate of particulate Mn(III/IV)-P and Fe(III)-P in the sulfidic deep waters. The sharp decline in particulate Mn that we observe in the lower part of redoxcline at our station ([Fig. 2](#)) is similar to the decrease in particulate Mn with water depth seen at other locations in the deep basin ([Lewis and Landing, 1991](#)). No particulate Mn was detected at 250 and 2000 mbss at our site by synchrotron μ XRF ([Fig. 4](#)) and the counts for Mn by SEM-EDS were very low ([Fig. 6](#)). The few Mn carbonate enrichments present at the sediment-water interface contained only little P ([Fig. 8](#)). These results show that Mn(III/IV)-P, the key pool of particulate P in the redoxcline, is subject to reductive dissolution in the deeper anoxic and sulfidic waters in the Black Sea and does not act as a carrier of P towards the sediments.

Similar to particulate Mn, most particulate Fe(III) in the Black Sea undergoes reductive dissolution within the upper part of the sulfidic water column, where it is converted to Fe(II)-sulfides ([Lewis and Landing, 1991](#); [Muramoto et al., 1991](#); [Lyons, 1997](#)). This is also observed at our station where pyrite is already present at 250 mbss (density of 16.8 $\delta\theta$; [Figs. 4–6](#)). Some particulate Fe(III) does, however, survive transport through the sulfidic water column. At our site, particulate Fe(III) is present at 250 and 2000 mbss ([Fig. 5](#)). At least part of this Fe(III) is present as Fe oxides and not as Fe(III)-rich clays since not all non-sulfidized Fe particles in the sulfidic waters contain elements associated with clays (e.g. Si, Al and K; [Fig. 6](#)). Whether Fe(III) is a relevant carrier of P towards the seafloor is estimated as follows:

$$\text{Fe(III) - P flux} = F_{\text{hr}} * f_{\text{Fe-ns}} * \left(\frac{1}{\text{Fe} : \text{P}_{\text{Fe(III)-P}}} \right) \quad (1)$$

where Fe(III)-P flux is the depositional flux of Fe oxide P, F_{hr} is the total flux of highly reactive Fe towards the seafloor in the deep basin, $f_{\text{Fe-ns}}$ is the fraction of highly reactive Fe that is not sulfidized, and $\text{Fe} : \text{P}_{\text{Fe(III)-P}}$ is the molar Fe:P ratio of settling Fe oxides with associated P. The values for F_{hr} and $f_{\text{Fe-ns}}$ were obtained from literature (6805 $\mu\text{mol Fe m}^{-2} \text{y}^{-1}$ and 9.6%, respectively; [Anderson and Raiswell, 2004](#)). We assumed an Fe:P ratio of 50:1 mol

mol^{-1} , which is the value for the Fe oxide from 2000 mbss (50:1 mol mol^{-1} ; [Fig. 6J](#)), that is also close to reported molar Fe:P ratios for crystalline Fe oxides (e.g. >30:1 mol mol^{-1} for goethite; [Galvez et al., 1999](#)). The Fe-oxides in the sulfidic deep waters likely consist of crystalline Fe oxides that are less reactive towards dissolved HS^- than poorly ordered, highly reactive Fe oxides ([Canfield et al., 1992](#)). The Fe:P values of the crystalline Fe-oxides are therefore assumed to be more representative for the Fe(III)-P in the sulfidic waters than the very low Fe:P ratio of particulate Fe(III)-P in the redoxcline. Our estimated Fe(III)-P flux is 13 $\mu\text{mol P m}^{-2} \text{y}^{-1}$, which contributes less than 1% of the total particulate P flux towards the seafloor in the deep basin of the Black Sea ([Table 2](#)). Some of the Fe(III) oxide P may be converted to Fe(II)-P phases such as ludlamite in the water column or sediment ($\text{Fe(II),Mg,Mn}_3(\text{PO}_4)_2 \cdot 4(\text{H}_2\text{O})$), but although some ludlamite was indeed present in the surface sediment at station 2 ([Kraal et al., 2017](#)), we did not detect it in the water column. Particulate Fe-P thus cannot explain the high CDB-extractable P concentrations in the sulfidic waters and in the surface sediments of the Black Sea ([Fig. 3](#) and [Table 2](#)).

4.4. P associated with CaCO_3 and clays in the water column and sediments

The exchangeable and CDB-extractable P pool in the surface sediments in the deep basin (5.6 $\mu\text{mol g}^{-1}$; [Fig. 3](#); [Table 2](#)) may represent P associated with CaCO_3 and, possibly, with clay ([Kraal et al., 2017](#)). This conclusion is supported by the correlation between P and Ca in the surface sediments at our site ([Fig. 8](#)). A role for vivianite inclusions in Deltaproteobacteria in explaining the CDB-extractable P pool in the deep basin sediments, as suggested previously ([Dijkstra et al., 2014](#)), can be excluded ([Appendix G](#)). However, the exchangeable and CDB-extractable P pool in the deep basin sediments ([Fig. 2](#) and [Appendix C](#)) cannot solely be attributed to surface adsorption onto CaCO_3 . This is apparent when comparing P sorption coefficients (K) for CaCO_3 from the literature to those calculated from the ratio of the exchangeable and CDB-extractable P pool ($\mu\text{mol g}^{-1}$) and the ambient porewater concentrations of PO_4 in Black Sea sediments ($\mu\text{mol mL}^{-1}$). If surface adsorption would account for all exchangeable and CDB-extractable P in the surface sediments, then the K value in the surface sediments would be 700 mL g^{-1} (porewater PO_4 concentrations of $\sim 8 \mu\text{M}$; [Appendix C](#)). This K value is higher than typical K values for CaCO_3 , most clays and anoxic sediments (1–100; [Edzwald et al., 1976](#); [Krom and Berner, 1980](#); [Millero et al., 2001](#)). Carbonated hydroxyapatite can also dissolve in the CDB-extraction step (31% of all extracted P; [Appendix F](#)). We thus conclude that the CDB-extractable P pool not only consists of P adsorbed onto CaCO_3 and clays but may also include labile Ca-P phases, possibly formed at CaCO_3 surfaces ([Wang et al., 2012](#)), that dissolve in the CDB-extraction step of the SEDEX procedure.

Adsorbed P or labile Ca-P may form in the water column and may be responsible for the particulate exchangeable and CDB-extractable P concentrations in the sulfidic

deep waters of ~ 4 nM (Ex-P and CDB-P, as extracted following the SEDEX procedure; Fig. 3). The fact that we did not find P on the CaCO_3 -rich exoskeletons from the water column (e.g. Fig. 6A) does not exclude CaCO_3 as an important carrier of P, as illustrated with the following calculation. If, for instance, 50% of the exchangeable and CDB-extractable P is deposited at the seafloor as CaCO_3 -associated P ($168 \mu\text{mol m}^{-2} \text{y}^{-1}$; Table 2) with a CaCO_3 deposition rate of $75 \text{ mmol m}^{-2} \text{y}^{-1}$ (Hay et al., 1990), then the fraction of P on the settling particulate CaCO_3 would be only 0.2 mol%. Even though these settling particles would make up a large P flux towards the sediments, it would be impossible to detect P on the investigated CaCO_3 particles by SEM-EDS.

Our ^{33}P radiotracer experiments show that adsorbed P and/or labile Ca-P can also form *in-situ* in deep basin sediments of the Black Sea (Fig. 9 and Table 3). This may explain the fast abiotic uptake of $^{33}\text{PO}_4$ in the CDB-extractable P fraction in the sediments. This uptake of ^{33}P is almost as rapid as the uptake of ^{33}P in the Fe oxide rich surface sediments on the Black Sea shelves (station 9; Table 3). We further notice a significant decrease in the ^{33}P activity in the exchangeable P fraction over 30 days (Fig. 9; Appendix E). This may reflect an abiotic sink-switching from easily adsorbed P (exchangeable P) to strongly adsorbed or labile Ca-P (CDB-extractable P). Adsorbed P and labile Ca-P may be converted into more stable authigenic Ca-P upon sediment burial. The P dynamics in the deep basin of the Black Sea are summarized in Fig. 10 and emphasize the role of adsorbed P, labile Ca-P and authigenic Ca-P as key burial phases in the deep basin

besides organic P. Detrital Ca-P plays only a minor role in the P dynamics in the deep basin of the Black Sea ($\sim 2\%$ of the deposited P; Table 2; Fig. 3).

5. IMPLICATIONS FOR P BURIAL IN EUXINIC BASINS

In this study, we show that most inorganic Mn-P-Fe particles and long-chained polyphosphates formed in the redoxcline of the Black Sea do not survive transport through the sulfidic waters to the seafloor (Fig. 10). Whether this also holds for other euxinic basins likely depends on the HS^- concentrations in the water column and the travel time of the particles before reaching the seafloor. In the Cariaco Basin, for instance, HS^- concentrations in the deep waters (1200 mbss) are an order of magnitude lower than in the deep basin of the Black Sea (40 versus $400 \mu\text{M}$; Fig. 2 and Taylor et al., 2001). As a consequence, more particulate Fe oxide P may survive transport through the water column, possibly explaining the large pool of exchangeable and CDB-extractable P in the sulfidic deep waters of the Cariaco Basin (McParland et al., 2015). Similarly, lower HS^- concentrations ($<75 \mu\text{M}$) and shorter travel times of particles to the seafloor (<437 mbss) allow the input of Fe oxide P to sediments of euxinic basins in the Baltic Sea (Jilbert and Slomp, 2013; Dijkstra et al., 2016; Reed et al., 2016). A good understanding of the transport of particles and their exposure to HS^- in the water column of euxinic basins is thus essential in determining whether Fe-Mn-P shuttling affects sedimentary P burial.

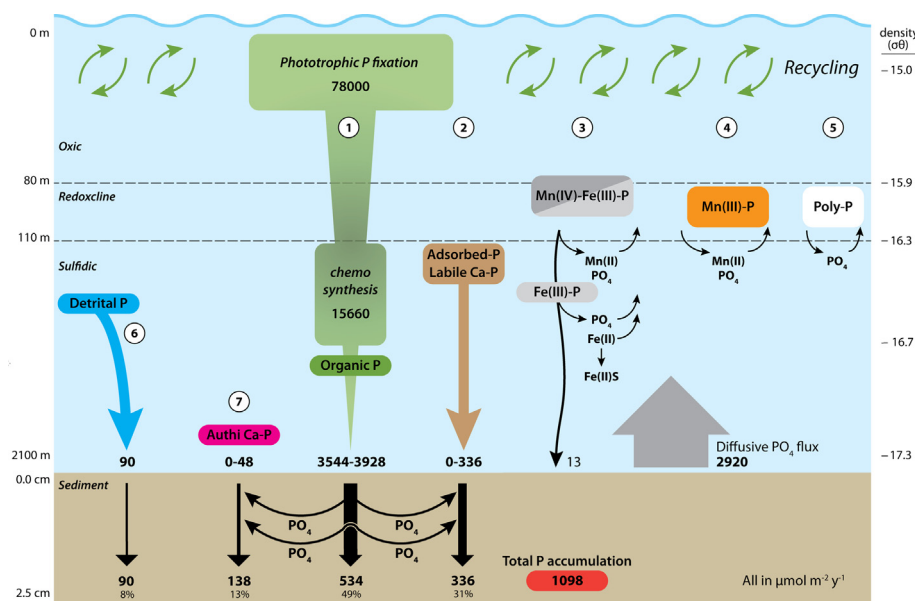


Fig. 10. Schematic overview of P dynamics in the water column and surface sediments in the Black Sea. Values are given in $\mu\text{mol P m}^{-2} \text{y}^{-1}$. Phototrophic P fixation and chemosynthesis result in a major flux of organic P towards the seafloor (1). The flux of adsorbed P and labile Ca-P (2) is assumed to be equal to at most $336 \mu\text{mol P m}^{-2} \text{y}^{-1}$ as some adsorbed P may in fact form in the surface sediments, presumably from PO_4 that is released by organic matter decomposition. Particulate Mn(IV)-Fe(III)-P forms in the redoxcline and a small proportion of the Fe(III)-P may escape sulfidization in the sulfidic waters (3). The $\text{Mn(III)-pyrophosphate}$ complexes and long-chain polyphosphates that form in the redoxcline are assumed to dissolve when entering the sulfidic water column (4–5). Some detrital apatite P may also be deposited onto the seafloor (6). Most authigenic Ca-P forms in the sediment (7).

Apart from periods of strongly enhanced Fe-transfer from shelves, e.g. linked to the onset of shelf hypoxia (Reed et al., 2016), organic P is still thought to be the main source of P to sediments in the euxinic basins of the Baltic Sea (Dijkstra et al., 2016; Reed et al., 2016). We show here that organic P may also dominates the input of P to the seafloor in the Black Sea. Preferential release of P relative to C from organic matter in the sulfidic deep waters and surface sediments, however, results in less burial of organic P than we expected based on C_{org} contents. While this finding contrasts with the preferential remineralization of P under oxic instead of anoxic conditions as reported for the Cariaco Basin water column (Benitez-Nelson et al., 2007), our results are in line with many previous studies that show preferential P release in sediments overlain by euxinic waters (e.g. Ingall et al., 1993; Van Cappellen and Ingall, 1997; Jilbert et al., 2011). This preferential release of P also explains the lower burial efficiency of organic P when compared to that of C_{org} in our Black Sea sediments (Table 2), as observed previously for Mediterranean sapropels (Slomp et al., 2002). The effect of preferential P release on sedimentary P burial should therefore be considered when studying the dynamics of P in anoxic and sulfidic basins.

We find that, besides organic matter, P associated with $CaCO_3$ may also be a quantitatively important P sink in sediments of euxinic basins. While the importance of $CaCO_3$ for sedimentary P burial was suggested previously for deep sea sediments (Morse and Cook, 1978; Froelich et al., 1982; De Lange, 1992), most $CaCO_3$ -P was later shown to be associated with Fe oxide coatings (Palmer, 1985; Sherwood et al., 1987; Ruttenberg, 2003). However, results of sequential extractions and ^{33}P -incubations of Fe oxide free, $CaCO_3$ -rich coastal sediments also suggest a rapid uptake of P by $CaCO_3$ and a possible sink-switching to Ca-P minerals (Jensen et al., 1998, 2009). Particularly in sediments where other mechanisms of inorganic P sequestration are less efficient, interactions of P with $CaCO_3$ may thus become relevant. Strikingly, the burial efficiency of total P in the deep basin sediments of the Black Sea is higher than that in the $CaCO_3$ -poor sediments in the Eastern Gotland Basin, a euxinic basin in the Baltic Sea (27% versus 0.2–12%; Viktorsson et al., 2013). We hypothesize that the presence of $CaCO_3$ may play a key role in P retention and possibly long-term sequestration by inducing Ca-P formation in sediments of euxinic basins, thereby reducing the recycling of P from the sediment.

ACKNOWLEDGEMENTS

This research was funded by the European Research Council under the European Community's Seventh Framework Programme for ERC Starting Grant #278364 to C.P. Slomp and the Netherlands Organisation for Scientific Research (Vici grant 865.13.005 and Open Competition grant 822.01013). Peter Kraal acknowledges Veni grant 863.14.014. We thank the captain, crew, scientists and technicians on board of RV Pelagia during the Black Sea cruises in 2013 and 2015. Patrick Laan is thanked for his assistance with the Flow-Injection system. We thank Fleur van Duyl and Milou Arts for their guidance and help with the inorganic polyphosphate measurements. The reviewers are thanked for their useful comments and suggestions. We thank Sam Webb for his

assistance at the 2-3 SSRL beam line and Edward D. Burton is thanked for his help during the XAS data collection at the SSRL. Use of the SSRL, SLAC National Accelerator Laboratory, is supported by the U.S. Department of Energy, Office of Science, Office of Basic Energy Sciences under Contract No. DE-AC02-76SF00515. The SSRL Structural Molecular Biology Program is supported by the DOE Office of Biological and Environmental Research, and by the National Institutes of Health, National Institute of General Medical Sciences (including P41GM103393). The contents of this publication are solely the responsibility of the authors and do not necessarily represent the official views of NIGMS or NIH.

APPENDICES A–G. SUPPLEMENTARY MATERIAL

Supplementary data associated with this article can be found, in the online version, at <https://doi.org/10.1016/j.gca.2017.11.016>.

REFERENCES

- Algeo T. J. and Ingall E. (2007) Sedimentary Corg: P ratios, paleocean ventilation, and Phanerozoic atmospheric pO_2 . *Palaeogeogr. Palaeoclimatol. Palaeoecol.* **256**, 130–155.
- Anderson T. and Raiswell R. (2004) Sources and mechanisms for the enrichment of highly reactive iron in euxinic Black Sea sediments. *Am. J. Sci.* **304**, 203–233.
- APHA (2005) *Standard methods for the examination of water and wastewater*. American Public Health Association – American Water Works Association – Water Environment Federation.
- Arthur M. A. and Dean W. E. (1998) Organic-matter production and preservation and evolution of anoxia in the Holocene Black Sea. *Paleoceanography* **13**, 395–411.
- Benitez-Nelson C. R., O'Neill Madden L., Styles R. M., Thunell R. C. and Astor Y. (2007) Inorganic and organic sinking particulate phosphorus fluxes across the oxic/anoxic water column of Cariaco Basin, Venezuela. *Mar. Chem.* **105**, 90–100.
- Borsboom M., Bras W., Cerjak I., Detollenaere D., Glastra van Loon D., Goedtkindt P., Konijnenburg M., Lassing P., Levine Y. K., Munneke B., Oversluisen M., van Tol R. and Vlieg E. (1998) The Dutch-Belgian beamline at the ESRF. *J. Synchrotron Rad.* **5**, 518–520.
- Brock J. and Schulz-Vogt H. N. (2011) Sulfide induces phosphate release from polyphosphate in cultures of a marine Beggiatoa strain. *ISME J.* **5**, 497–506.
- Burdige D. and Neelson K. (1986) Chemical and microbiological studies of sulfide-mediated manganese reduction 1. *Geomicrobiol. J.* **4**, 361–387.
- Calvert S., Thode H., Yeung D. and Karlin R. (1996) A stable isotope study of pyrite formation in the Late Pleistocene and Holocene sediments of the Black Sea. *Geochim. Cosmochim.* **60**, 1261–1270.
- Canfield D. (1989) Sulfate reduction and oxic respiration in marine sediments: implications for organic carbon preservation in euxinic environments. *Deep Sea Res. Part A. Oceanogr. Res.* **36**, 121–138.
- Canfield D., Raiswell R. and Bottrell S. (1992) The reactivity of sedimentary iron minerals toward sulfide. *Am. J. Sci.* **292**, 659–683.
- Carstensen J., Andersen J. H., Gustafsson B. G. and Conley D. J. (2014) Deoxygenation of the Baltic Sea during the last century. *Proc. Natl. Acad. Sci. USA* **111**, 5628–5633.
- Coban-Yildiz Y., Chiavari G., Fabbri D., Gaines A. F., Galletti G. and Tugrul S. (2000) The chemical composition of Black Sea

- suspended particulate organic matter: pyrolysis-GC/MS as a complementary tool to traditional oceanographic analyses. *Mar. Chem.* **69**, 55–67.
- Conley D. J., Björck S., Bonsdorff E., Carstensen J., Destouni G., Gustafsson B. G., Hietanen S., Kortekaas M., Kuosa H., Markus Meier H. E., Müller-Karulis B., Nordberg K., Norkko A., Nürnberg G., Pitkänen H., Rabalais N. N., Rosenberg R., Savchuk O. P., Slomp C. P., Voss M., Wulff F. and Zillén L. (2009) Hypoxia-related processes in the Baltic Sea. *Environ. Sci. Technol.* **43**, 3412–3420.
- Crusius J. and Anderson R. (1992) Inconsistencies in Accumulation Rates of Black Sea Sediments Inferred from Records of Laminae and ²¹⁰Pb. *Paleoceanography* **7**, 215–227.
- Davies G. (1969) Some aspects of the chemistry of manganese(III) in aqueous solution. *Coord. Chem. Rev.* **4**, 199–224.
- De Baar H., Timmermans K., Laan P., Porto H., Ober S., Blom J. J., Bakker M. C., Schilling J., Sarthou G., Smit M. G. and Klunder M. (2008) Titan: A new facility for ultraclean sampling of trace elements and isotopes in the deep oceans in the international Geotraces program. *Mar. Chem.* **111**, 4–21.
- Degens E. T. and Ross D. A. (1974) The Black Sea—Geology, Chemistry, and Biology.
- De Jonge V. N. and Villerius L. A. (1989) Possible role of carbonate dissolution in estuarine phosphate dynamics. *Limnol. Oceanogr.* **34**, 332–340.
- De Lange G. J. (1992) Distribution of various extracted phosphorus compounds in the interbedded turbiditic/pelagic sediments of the Madeira Abyssal Plain, eastern North Atlantic. *Mar. Geol.* **109**, 115–139.
- Dellwig O., Leipe T., März C., Glockzin M., Pollehne F., Schnetger B., Yakushev E. V., Böttcher M. E. and Brumsack H.-J. (2010) A new particulate Mn–Fe–P-shuttle at the redoxcline of anoxic basins. *Geochim. Cosmochim. Acta* **74**, 7100–7115.
- Deuser W. G. (1971) Organic-carbon budget of the Black Sea. *Deep Sea Res. Oceanogr. Abstr.* **18**, 995–1004.
- Diaz J. M., Ingall E. D., Snow S. D., Benitez-Nelson C. R., Taillefert M. and Brandes J. a. (2012) Potential role of inorganic polyphosphate in the cycling of phosphorus within the hypoxic water column of Effingham Inlet, British Columbia. *Global Biogeochem. Cycles* **26**.
- Diaz J. M., Björkman K. M., Haley S. T., Ingall E. D., Karl D. M., Longo A. F. and Dyhrman S. T. (2016) Polyphosphate dynamics at Station ALOHA, North Pacific subtropical gyre. *Limnol. Oceanogr.* **61**, 227–239.
- Diaz R. J. and Rosenberg R. (2008) Spreading dead zones and consequences for marine ecosystems. *Science* **321**, 926–929.
- Dijkstra N., Kraal P., Kuypers M. M. M., Schnetger B. and Slomp C. P. (2014) Are iron-phosphate minerals a sink for phosphorus in anoxic Black Sea sediments? *PLoS ONE* **9**, e101139.
- Dijkstra N., Slomp C. P., Behrends T. and Expedition 347 scientists (2016) Vivianite is a key sink for phosphorus in sediments of the Landsort Deep, an intermittently anoxic deep basin in the Baltic Sea. *Chem. Geol.* **438**, 58–72.
- Edzwald J. K., Toensing D. C. and Leung M. C.-Y. (1976) Phosphate adsorption reactions with clay minerals. *Environ. Sci. Technol.* **10**, 485–490.
- Paul K. L., Paytan A. and Delaney M. L. (2005) Phosphorus distribution in sinking oceanic particulate matter. *Mar. Chem.* **97**, 307–333.
- Froelich P., Bender M. and Luedtke N. (1982) The marine phosphorus cycle. *Am. J. Sci.* **282**, 474–511.
- Fry B., Jannasch H., Molyneux S., Wirsén C., Muramoto J. A. and King S. (1991) Stable isotope studies of the carbon, nitrogen and sulfur cycles in the Black Sea and the Cariaco Trench. *Deep Sea Res. Part A. Oceanogr. Res. Pap.* **38**, S1003–S1019.
- Galvez N., Barron V. and Torrent J. (1999) Preparation and properties of hematite with structural phosphorus. *Clays Clay Miner.* **47**, 375–385.
- Goldhammer T., Brüchert V., Ferdelman T. G. and Zabel M. (2010) Microbial sequestration of phosphorus in anoxic upwelling sediments. *Nat. Geosci.* **3**, 557–561.
- Golubev S. V., Pokrovsky O. S. and Savenko V. S. (2001) Homogeneous precipitation of magnesium phosphates from seawater solutions. *J. Cryst. Growth* **223**, 550–556.
- Grasshoff K., Ehrhardt M. and Kremling K. eds. (1983) *Methods of seawater analysis*. Second., Weinheim/Deerfield Beach, Florida, Verlag Chemie.
- Hay B. J., Honjo S., Kempe S., Ittekkot V. A., Degens E. T., Konuk T. and Izdar E. (1990) Interannual variability in particle flux in the southwestern Black Sea. *Deep Sea Res. Part A. Oceanogr. Res. Pap.* **37**, 911–928.
- Ingall E. D., Bustin R. M. and Van Cappellen P. (1993) Influence of water column anoxia on the burial and preservation of carbon and phosphorus in marine shales. *Geochim. Cosmochim. Acta* **57**, 303–316.
- Jensen H. S., Mortensen P. B., Andersen F., Rasmussen E. and Jensen A. (1995) Phosphorus cycling in a coastal marine sediment, Aarhus Bay, Denmark. *Limnol. Oceanogr.* **40**, 908–917.
- Jensen H., McGlathery K., Marino R. and Howarth R. W. (1998) Forms and availability of sediment phosphorus in carbonate sand of Bermuda seagrass beds. *Limnol. Oceanogr.* **43**, 799–810.
- Jensen H. S., Nielsen O. I., Koch M. S. and de Vicente I. (2009) Phosphorus release with carbonate dissolution coupled to sulfide oxidation in Florida Bay seagrass sediments. *Limnol. Oceanogr.* **54**, 1753–1764.
- Jilbert T. and Slomp C. P. (2013) Iron and manganese shuttles control the formation of authigenic phosphorus minerals in the euxinic basins of the Baltic Sea. *Geochim. Cosmochim. Acta* **107**, 155–169.
- Jilbert T., Slomp C. P., Gustafsson B. G. and Boer W. (2011) Beyond the Fe–P–redox connection: preferential regeneration of phosphorus from organic matter as a key control on Baltic Sea nutrient cycles. *Biogeochemistry* **8**, 1699–1720.
- Johnson K., Elrod V., Fitzwater S. and Plant J. (2007) Developing standards for dissolved iron in seawater. *Eos, Trans.*
- Jørgensen B. B., Fossing H., Wirsén C. O. and Jannasch H. W. (1991) Sulfide oxidation in the anoxic Black Sea chemocline. *Deep Sea Res. Part A. Oceanogr. Res. Pap.* **38**, S1083–S1103.
- Klunder M. B., Laan P., Middag R., De Baar H. J. W. and Van Ooijen J. C. (2011) Dissolved iron in the Southern Ocean (Atlantic sector). *Deep Sea Res. Part II Top. Stud. Oceanogr.* **58**, 2678–2694.
- Kornberg A. (1995) Inorganic polyphosphate: toward making a forgotten polymer unforgettable. *J. Bacteriol.* **177**, 491–496.
- Kostka J. E., Luther G. W. and Nealson K. H. (1995) Chemical and biological reduction of Mn(III)-pyrophosphate complexes: Potential importance of dissolved Mn(III) as an environmental oxidant. *Geochim. Cosmochim. Acta* **59**, 885–894.
- Kraal P., Dijkstra N., Behrends T. and Slomp C. P. (2017) Phosphorus burial in sediments of the sulfidic deep Black Sea: key roles for adsorption by calcium carbonate and apatite authigenesis. *Geochim. Cosmochim. Acta* **204**, 140–158.
- Krom M. D. and Berner R. A. (1980) Adsorption of phosphate in anoxic marine sediments. *Limnol. Oceanogr.* **25**, 797–806.
- Lewis B. L. and Landing W. M. (1991) The biogeochemistry of manganese and iron in the Black Sea. *Deep Sea Res. Part A. Oceanogr. Res. Pap.* **38**, S773–S803.

- Lyons T. W. (1997) Sulfur isotopic trends and pathways of iron sulfide formation in upper Holocene sediments of the anoxic Black Sea. *Geochim. Cosmochim. Acta* **61**, 3367–3382.
- Martin P., Dyhrman S. T., Lomas M. W., Poulton N. J. and Van Mooy B. A. S. (2014) Accumulation and enhanced cycling of polyphosphate by Sargasso Sea plankton in response to low phosphorus. *Proc. Natl. Acad. Sci. USA* **111**, 8089–8094.
- Martin P. and Van Mooy B. A. S. (2013) Fluorometric quantification of polyphosphate in environmental plankton samples: Extraction protocols, matrix effects, and nucleic acid interference. *Appl. Environ. Microbiol.* **79**, 273–281.
- McParland E., Benitez-Nelson C. R., Taylor G. T., Thunell R., Rollings A. and Lorenzoni L. (2015) Cycling of suspended particulate phosphorus in the redoxcline of the Cariaco Basin. *Mar. Chem.* **176**, 64–74.
- Millero F., Huang F., Zhu X., Liu X. and Zhang J. (2001) Adsorption and desorption of phosphate on calcite and aragonite in seawater. *Aquat. Geochem.* **7**, 33–56.
- Morse J. W. and Cook N. (1978) The distribution and form of phosphorus in North Atlantic Ocean deep-sea and continental slope sediment 1. *Limnol. Oceanogr.* **23**, 825–830.
- Mort H. P., Slomp C. P., Gustafsson B. G. and Andersen T. J. (2010) Phosphorus recycling and burial in Baltic Sea sediments with contrasting redox conditions. *Geochim. Cosmochim. Acta* **74**, 1350–1362.
- Muramoto J. A., Honjo S., Fry B., Hay B. J., Howarth R. W. and Cisne J. L. (1991) Sulfur, iron and organic carbon fluxes in the Black Sea: sulfur isotopic evidence for origin of sulfur fluxes. *Deep Sea Res. Part A. Oceanogr. Res. Pap.* **38**, S1151–S1187.
- Murphy J. and Riley J. P. (1962) A modified single solution method for the determination of phosphate in natural waters. *Anal. Chim. Acta* **27**, 31–36.
- Murray J. W. and Yakushev E. (2006) The suboxic transition zone in the Black Sea. In *Past and Present Water Column Anoxia*. Kluwer Academic Publishers, Dordrecht, pp. 105–138.
- Nembrini G. P., Capobianco J. A., Viel M. and Williams A. F. (1983) A Mössbauer and chemical study of the formation of vivianite in sediments of Lago Maggiore (Italy). *Geochim. Cosmochim. Acta* **47**, 1459–1464.
- Nikitenko S., Beale A., Van der Eerden A. M. J., Jacques S. D. M., Leynaud O., O'Brien M. G., Detollenaere D., Kaptein R., Weckhuysen B. M. and Bras W. (2008) Implementation of a combined SAXS/WAXS/QEXAFS set-up for time-resolved in situ experiments. *J. Synchrotron Radiat.* **15**, 632–640.
- Oguz T. and Merico A. (2006) Factors controlling the summer *Emiliania huxleyi* bloom in the Black Sea: a modeling study. *J. Mar. Syst.* **59**, 173–188.
- Pakhomova S. V., Rozanov A. G. and Yakushev E. V. (2009) Dissolved and particulate forms of iron and manganese in the redox zone of the Black Sea. *Oceanology* **49**, 773–787.
- Palmer M. R. (1985) Rare earth elements in foraminifera tests. *Earth Planet. Sci. Lett.* **73**, 285–298.
- Rabalais N. N., Cai W.-J., Carstensen J., Conley D. J., Fry B., Hu X., Quiñones-Rivera Z., Rosenberg R., Slomp C. P., Turner R. E., Voss M., Wissel B. and Zhang J. (2014) Eutrophication-driven deoxygenation in the coastal ocean. *Oceanography* **27**(1), 172–183. <https://doi.org/10.5670/oceanog.2014.21>.
- R Core Team (2016) R: A language and environment for statistical computing.
- Ravel B. and Newville M. (2005) ATHENA, ARTEMIS, HEPHAESTUS: data analysis for X-ray absorption spectroscopy using IFEFFIT. *J. Synchrotron Radiat.* **12**, 537–541.
- Redfield A. C. (1958) The biological control of chemical factors in the environment. *Am. Sci.* **46**, 205–221.
- Reed D. C., Gustafsson B. G. and Slomp C. P. (2016) Shelf-to-basin iron shuttling enhances vivianite formation in deep Baltic Sea sediments. *Earth Planet. Sci. Lett.* **434**, 241–251.
- Rijkenberg M. J., Middag R., Laan P., Gerringa L. J., Van Aken H. M., Schoemann V., De Jong J. T. and De Baar H. J. (2014) The distribution of dissolved iron in the West Atlantic Ocean. *PLoS ONE* **9**, e101323.
- Ross D. and Degens E. (1974) Recent sediments of Black Sea. In *The Black Sea-Geology, chemistry, and Biology* pp. 183–199.
- Ruttenberg K. C. (1992) Development of a sequential extraction method for different forms of phosphorus in marine sediments. *Limnol. Oceanogr.* **37**, 1460–1482.
- Ruttenberg K. C. (2003) The global phosphorus cycle. *Treatise Geochem.* **8**, 585–643.
- Sanchez-Cabeza J. A. and Ruiz-Fernández A. C. (2012) 210Pb sediment radiochronology: An integrated formulation and classification of dating models. *Geochim. Cosmochim. Acta* **82**, 183–200.
- Sannigrahi P. and Ingall E. (2005) Polyphosphates as a source of enhanced P fluxes in marine sediments overlain by anoxic waters: Evidence from 31 P NMR. *Geochem. Trans.* **6**, 52–59.
- Schenau S. J. and De Lange G. J. (2000) A novel chemical method to quantify fish debris in marine sediments. *Limnol. Oceanogr.* **45**, 963–971.
- Schulz H. N. and Schulz H. D. (2005) Large sulfur bacteria and the formation of phosphorite. *Science* **307**, 416–418.
- Scranton M. I., Astor Y., Bohrer R., Ho T.-Y. and Muller-Karger F. (2001) Controls on temporal variability of the geochemistry of the deep Cariaco Basin. *Deep Sea Res. Part I Oceanogr. Res. Pap.* **48**, 1605–1625.
- Shaffer G. (1986) Phosphate pumps and shuttles in the Black Sea. *Nature* **321**, 515–517.
- Sherwood B. A., Sager S. L. and Holland H. D. (1987) Phosphorus in foraminiferal sediments from North Atlantic Ridge cores and in pure limestones. *Geochim. Cosmochim. Acta* **51**, 1861–1866.
- Slomp C. P., Epping E. H. G., Helder W. and Van Raaphorst W. (1996) A key role for iron-bound phosphorus in authigenic apatite formation in North Atlantic continental platform sediments. *J. Mar. Res.* **54**, 1179–1205.
- Slomp C. P., Thomson J. and De Lange G. J. (2002) Enhanced regeneration of phosphorus during formation of the most recent eastern Mediterranean sapropel (S1). *Geochim. Cosmochim. Acta* **66**, 1171–1184.
- Sorokin Y., Sorokin P., Avdeev V., Sorokin D. and Ilchenko S. (1995) Biomass production and activity in the Black Sea, with special reference to chemosynthesis and sulfur cycle. *Hydrobiologia* **308**, 61–76.
- Steenbergh A. K., Bodelier P. L. E., Heldal M., Slomp C. P. and Laanbroek H. J. (2013) Does microbial stoichiometry modulate eutrophication of aquatic ecosystems? *Environ. Microbiol.* **15**, 1572–1579.
- Steenbergh A. K., Bodelier P. L. E., Hoogveld H. L., Slomp C. P. and Laanbroek H. J. (2011) Phosphatases relieve carbon limitation of microbial activity in Baltic Sea sediments along a redox-gradient. *Limnol. Oceanogr.* **56**, 2018–2026.
- Strickland T. D. H. and Parsons T. R. (1972) A Practical Handbook of Seawater Analysis.
- Sun M. Y. and Wakeham S. G. (1994) Molecular evidence for degradation and preservation of organic matter in the anoxic Black Sea Basin. *Geochim. Cosmochim. Acta* **58**, 3395–3406.
- Taylor G. T., Iabichella M., Ho T.-Y., Scranton M. I., Thunell R. C., Muller-Karger F. and Varela R. (2001) Chemoautotrophy in the redox transition zone of the Cariaco Basin: a significant midwater source of organic carbon production. *Limnol. Oceanogr.* **46**, 148–163.

- Tebo B. M. (1991) Manganese(II) oxidation in the suboxic zone of the Black Sea. *Deep Sea Res. Part A. Oceanogr. Res. Pap.* **38**, S883–S905.
- Tebo B. M., Bargar J. R., Clement B. G., Dick G. J., Murray K. J., Parker D., Verity R. and Webb S. M. (2004) Biogenic manganese oxides: properties and mechanisms of formation. *Annu. Rev. Earth Planet. Sci.* **32**, 287–328.
- Tolmazin D. (1985) Changing coastal oceanography of the Black Sea. I: Northwestern shelf. *Prog. Oceanogr.* **15**, 217–276.
- Trouwborst R. E., Clement B. G., Tebo B. M., Glazer B. T. and Luther G. W. (2006) Soluble Mn(III) in suboxic zones. *Science* **313**, 1955–1957.
- Van Cappellen P. and Ingall E. D. (1997) Response to comment: “redox stabilization of the atmosphere and oceans and marine productivity” by A.S. Colman, F.T. Mackenzie and H.D. Holland. *Science* **275**, 407–408.
- Viktorsson L., Ekeröth N., Nilsson M., Kononets M. and Hall P. O. J. (2013) Phosphorus recycling in sediments of the central Baltic Sea. *Biogeosciences* **10**, 3901–3916.
- Wakeham S. G., Amann R., Freeman K. H., Hopmans E. C., Jørgensen B. B., Putnam I. F., Schouten S., Sinninghe Damsté J. S., Talbot H. M. and Woebken D. (2007) Microbial ecology of the stratified water column of the Black Sea as revealed by a comprehensive biomarker study. *Org. Geochem.* **38**, 2070–2097.
- Wang L., Ruiz-Agudo E., Putnis C. V., Menneken M. and Putnis A. (2012) Kinetics of calcium phosphate nucleation and growth on calcite: implications for predicting the fate of dissolved phosphate species in alkaline soils. *Environ. Sci. Technol.* **46**, 834–842.
- Wijsman J., Middelburg J. and Heip C. (2001) Reactive iron in Black Sea sediments: implications for iron cycling. *Mar. Geol.* **172**, 167–180.
- Wilkin R. T., Arthur M. A. and Dean W. E. (1997) History of water-column anoxia in the Black Sea indicated by pyrite framboid size distributions. *Earth Planet. Sci. Lett.* **148**, 517–525.
- Yakushev E. V., Pollehne F., Jost G., Kuznetsov I., Schneider B. and Umlauf L. (2007) Analysis of the water column oxic/anoxic interface in the Black and Baltic seas with a numerical model. *Mar. Chem.* **107**, 388–410.
- Yakushev E., Pakhomova S., Sørensen K. and Skei J. (2009) Importance of the different manganese species in the formation of water column redox zones: observations and modeling. *Mar. Chem.* **117**, 59–70.
- Yilmaz A., Çoban-Yildiz Y., Telli-Karakoç F. and Bologa A. (2006) Surface and mid-water sources of organic carbon by photoautotrophic and chemoautotrophic production in the Black Sea. *Deep Res. Part II Top. Stud. Oceanogr.* **53**, 1988–2004.

Associate editor: Thomas Wagner